

Longer-term terrestrial responses in the aftermath of the end-Cretaceous mass extinction

Jingyu Wang¹, Xianghui Li¹, Yongxiang Li¹, Yin Wang², and Chengyu Zheng¹

¹Nanjing University

²East China Mineral Exploration and Development Bureau

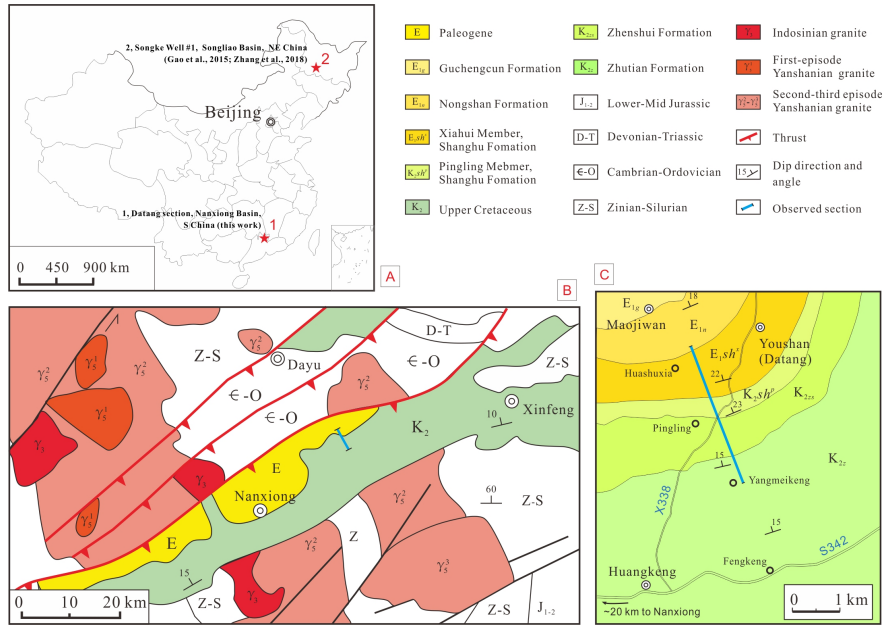
February 20, 2023

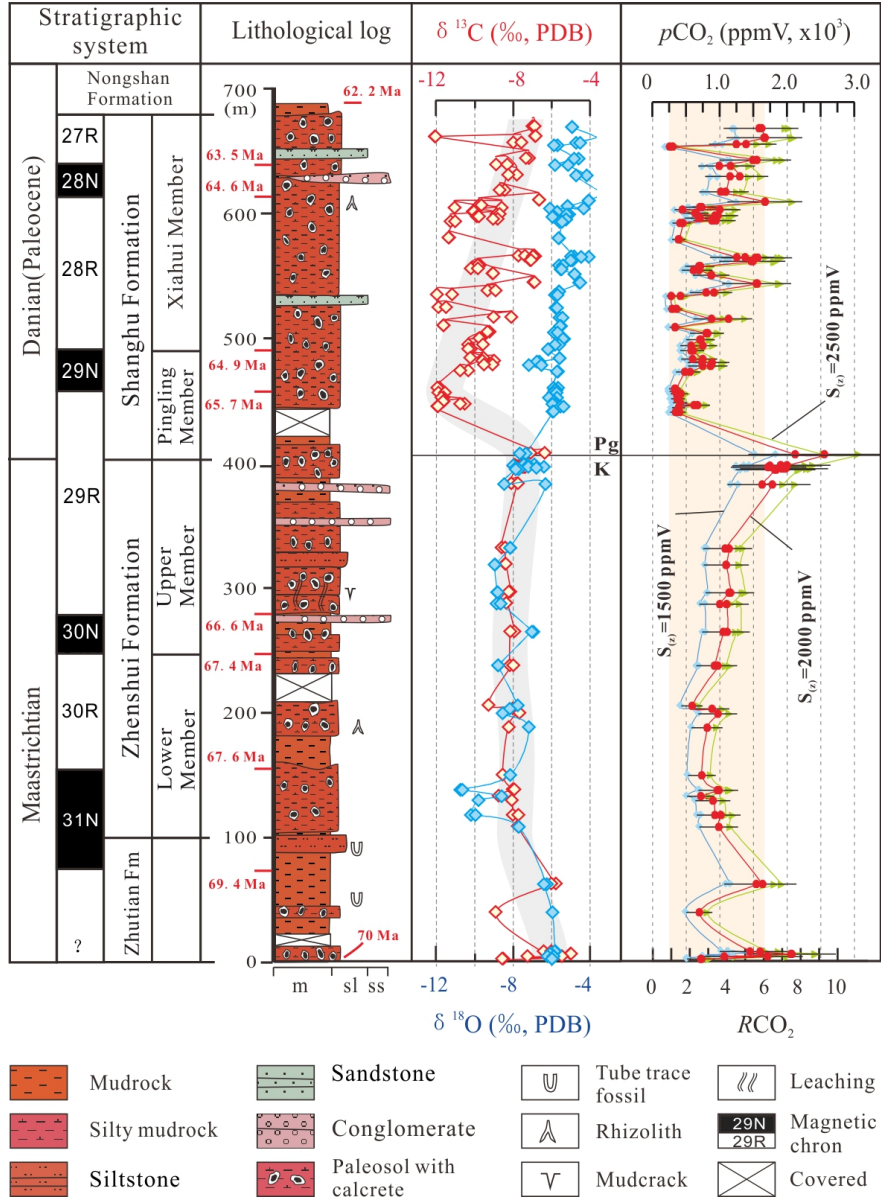
Abstract

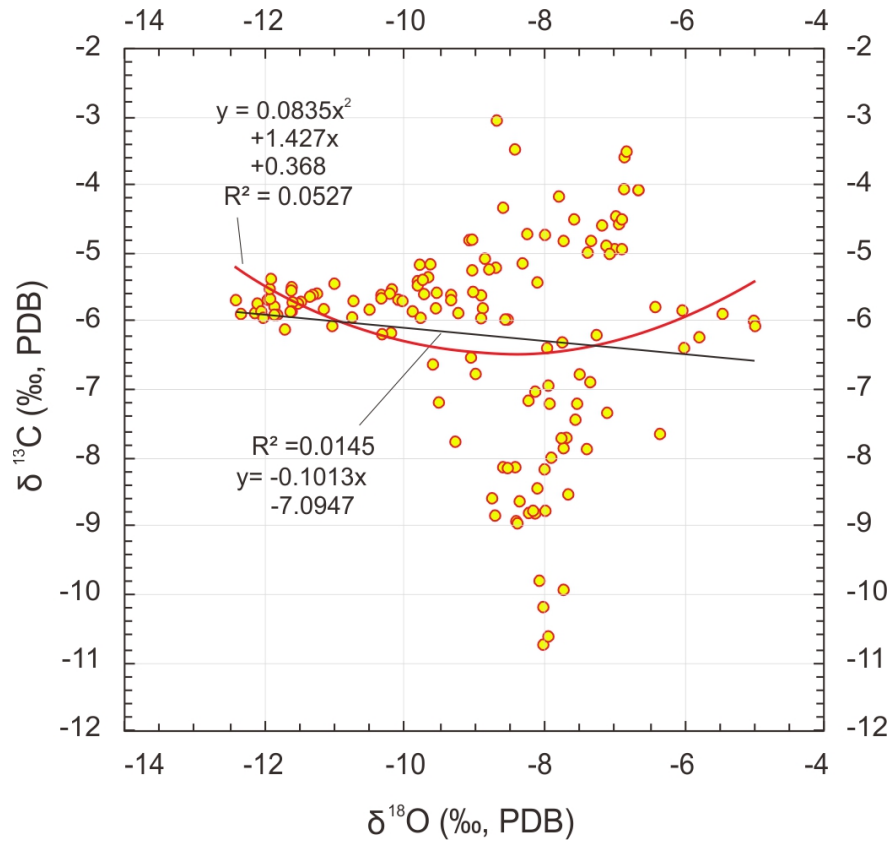
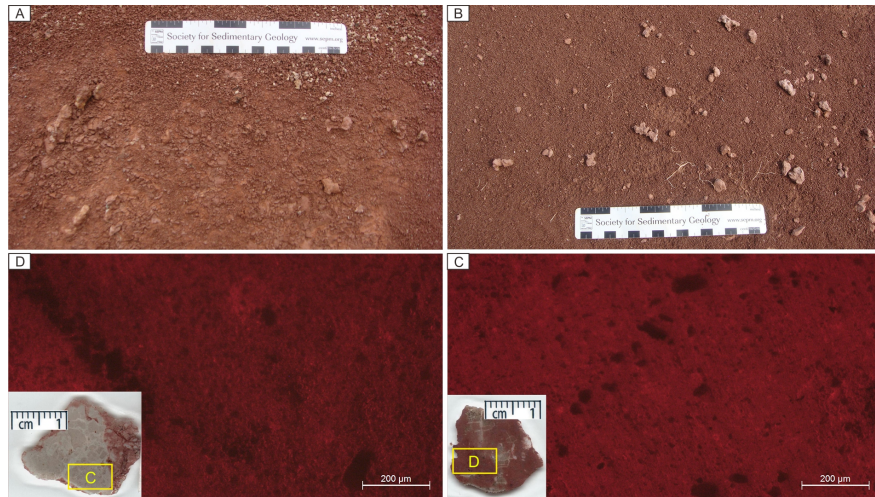
Mass-extinction with instantaneous and short-term effects on extreme climate and deteriorated ocean environment across the Cretaceous/Paleogene boundary (K/PgB) has been verified by an array of geological records, however, a longer-term (~100-1000 Kyr) post-K/PgB variation remain poorly understood, particularly due to the scarcity of terrestrial records. This study presents carbon isotope analyses of pedogenic carbonates in the Nanxiong Basin, South China to reconstruct carbon cycles and atmospheric CO₂ concentrations ($p\text{CO}_2$) spanning 70.0–62.0 Ma. Combined with data from Songliao Basin (China) and Tornillo Basin (USA), $\delta^{13}\text{C}$ displays a post-K/PgB (66.0-64.5 Ma) vibration that is correlative to the surface ocean but mirroring to the bottom ocean. The vibration shows a pattern of collapse and smooth towards rebound, constituting a process of ~400 Kyr (millennia) deterioration, ~300 Kyr stabilization and ~800 Kyr recovery for the longer-term ecosystem and environment. A similar pattern is observed for the reconstructed $p\text{CO}_2$, correlating to changes of sea surface temperature (SST) but contrasting bottom water temperature (BWT). With the discrepancy of longer-term proxy variations, it is proposed that ecosystems and environments in terrestrial and surface ocean had experienced a more unstable, difficult and erratic recovery process and were much more sensitive to climatic changes than in deep ocean for ~1.5 million years in the aftermath of the end-Cretaceous mass extinction. In addition, the decoupling of proxy variations from expected effects implies Deccan volcanism and Chicxulub impact may not have played a key role in the longer-term CO₂ perturbation and environmental change following the K/PgB.

Hosted file

956424_0_art_file_10716905_rq6xgp.docx available at <https://authorea.com/users/587417/articles/625127-longer-term-terrestrial-responses-in-the-aftermath-of-the-end-cretaceous-mass-extinction>







1 **Longer-term terrestrial responses in the aftermath of the end-Cretaceous**
2 **mass extinction**

3
4 **J. Y. Wang¹, X. H. Li¹, Y. X. Li¹, Y. Wang², and C. Y. Zheng¹**

5
6 ¹State Key Laboratory of Mineral Deposit Research, School of Earth Sciences and Engineering
7 Nanjing University, Nanjing 210023, China

8 ²East China Mineral Exploration and Development Bureau of Jiangsu Province, Nanjing
9 210007, China

10
11 Corresponding author: Xianghui Li (seanlee@nju.edu.cn)

12
13 **Key Points (each 140 characters limit):**

- 14 ● Terrestrial carbon isotope and $p\text{CO}_2$ vibrate by collapse, smooth and rebound in 1.5
15 million years after Cretaceous/Paleogene boundary
- 16 ● With similar pattern in surface ocean, vibrations unravel a process of deterioration,
17 stabilization and recovery of global ecosystem
- 18 ● Terrestrial and surface ocean systems experienced more unstable, difficult and erratic
19 recovery process than in deep ocean system

20
21

22 **Abstract**

23 Mass-extinction with instantaneous and short-term effects on extreme climate and
24 deteriorated ocean environment across the Cretaceous/Paleogene boundary (K/PgB) has been
25 verified by an array of geological records, however, a longer-term (~100–1000 Kyr)
26 post-K/PgB variation remains poorly understood, particularly due to the scarcity of terrestrial
27 records. This study presents carbon isotope analysis of pedogenic carbonates in the Nanxiong
28 Basin, South China to reconstruct carbon cycles and atmospheric CO₂ concentrations (*p*CO₂)
29 spanning 70.0–62.0 Ma. Combined with data from Songliao Basin (China) and Tornillo Basin
30 (USA), δ¹³C displays a post-K/PgB (66.0–64.5 Ma) vibration that is correlative to the surface
31 ocean but mirroring to the bottom ocean. The vibration shows a pattern of collapse and
32 smooth towards rebound, constituting a process of ~400 Kyr (millennia) deterioration, ~300
33 Kyr stabilization and ~800 Kyr recovery for the longer-term ecosystem and environment. A
34 similar pattern is observed for the reconstructed *p*CO₂, correlating to changes of sea surface
35 temperature (SST) but contrasting bottom water temperature (BWT). With the discrepancy of
36 longer-term proxy variations, it is proposed that ecosystems and environments in terrestrial
37 and surface ocean had experienced a more unstable, difficult and erratic recovery process and
38 were much more sensitive to climatic changes than in deep ocean for ~1.5 million years in the
39 aftermath of the end-Cretaceous mass extinction. In addition, the decoupling of proxy
40 variations from expected effects implies Deccan volcanism and Chicxulub impact may not
41 have played a key role in the longer-term CO₂ perturbation and environmental change
42 following the K/PgB.

43

44 **Keywords:** pedogenic carbonate; carbon cycle; atmospheric CO₂ concentration; ecosystem;
45 climatic perturbation; Cretaceous-Paleogene boundary

46

47 **Plain Language Summary**

48 The end-Cretaceous mass extinction is well known for the demise of non-avian dinosaurs
49 at ~66 Ma (million years ago). The instantaneous (< ~1.0 Kyr; thousands years) extreme
50 changes of environment and climate with the mass extinction have been attributed to the
51 Chicxulub impact and recently linked to the Indian Deccan volcanism. However, longer-term
52 (>100 Kyr) changes of environmental and climatic conditions across the
53 Cretaceous/Paleogene boundary (K/PgB) remain poorly understood, especially in terrestrial
54 realm. In this paper, a terrestrial record from South China combined with data from Northeast
55 China and America is presented to decipher climate conditions using carbon isotope (δ¹³C) of
56 pedogenic carbonates and estimated atmospheric CO₂ concentration (*p*CO₂). Results show
57 that δ¹³C and *p*CO₂ changes are characterized by collapse, smooth and rebound spanning ~1.5
58 million years after the K/PgB, indicating the deterioration, stabilization and recovery of
59 terrestrial ecosystem. With correlatability in surface sea and mirroring in deep ocean,
60 terrestrial and surface ocean ecosystems probably experienced a more difficult and erratic
61 recovery process than deep water, appearing at odds with the expected effects of geological
62 events, suggesting Chicxulub impact and Deccan volcanism may not have played the key role
63 in longer-term CO₂ perturbation and environmental change.

64

65 1. Introduction

66 As one of the five largest mass extinctions of the Phanerozoic (e.g., Keller, 1988, 2014),
67 the end-Cretaceous mass extinction is best known for the demise of non-avian dinosaurs. The
68 Chicxulub asteroid impact and Deccan volcanism have been speculated as crucial events that
69 drove climate deterioration (e.g., Alvarez, et al., 1980; Hildebrand et al., 1991; Nordt et al.,
70 2002; 2003; Vajda et al., 2003; Keller, 2014; Keller et al., 2012, 2020; Barnet et al., 2018;
71 Zhang et al., 2018; Gilabert et al., 2021b) and the mass extinction (e.g., MacLeod et al., 1998;
72 Schulte et al., 2010; Renne et al., 2015; Hull et al., 2020; and references therein), even though
73 the precise driving mechanism and the role that each event played in the mass extinction are
74 still strongly debated (e.g., Keller et al., 2016; Percival et al., 2018; Sprain et al., 2019;
75 Dzombak et al., 2020; Gilabert et al., 2021a, b).

76 Consequently, transient ($< \sim 1$ Kyr, millennia years) deterioration and recovery of
77 ecosystem, environment and climate immediately following the Cretaceous/Paleogene
78 boundary (K/PgB) have been well illustrated in marine environment anomalies in temperature
79 (e.g., Vellekoop et al., 2016; Woelders et al., 2017; Barnet et al., 2018), bioproductivity (e.g.,
80 Donovan et al., 2016; Henehan et al., 2016), surface ocean acidification (D'Hondt et al.,
81 1994; Kring, 2007; Ohno et al., 2014; Tyrrell et al., 2015; Hart et al., 2019; Henehan et al.
82 2019), methane emission (Beerling et al 2002), extinction of pelagic calcifiers (e.g., D'Hondt
83 and Keller, 1991; Bown, 2005), food web collapse (Coccioni and Marsili, 2007), carbonate
84 dissolution (Coccioni et al., 2012; Henehan et al., 2016); and also in the terrestrial realm by
85 biota (e.g., Vajda et al., 2001; Wilf et al., 2003; Coccioni and Marsili, 2007), geochemistry
86 (e.g., Sepúlveda et al., 2009; Nordt et al., 2011; Gao et al., 2021), carbon and oxygen isotopes
87 (Nordt et al., 2002, 2003; Gao et al., 2015; Zhang et al., 2018), subaerial temperature (Nordt
88 et al., 2003; Dworkin et al., 2005; Zhang et al., 2018), atmospheric CO₂ concentrations (i.e.
89 the partial pressure, $p\text{CO}_2$; e.g., Arens et al., 2000; Nordt et al., 2002, 2003; Gao et al., 2015),
90 magnetic susceptibility (Ma et al., 2018), total Hg/TOC ratios (e.g., Keller et al., 2020; Zhao,
91 et al., 2021; Gu et al. 2022; Ma et al., 2022), and so on.

92 On the other hand, a longer-term ($\sim 100\text{--}1000$ Kyr interval) environment and climate
93 change in the aftermath of the end-Cretaceous mass extinction has not been extensively
94 explored due to the lack of suitable materials, leading to a poor understanding of intrinsic
95 linkages in global environment and climate changes to causal mechanism. To date, there are
96 few examples of climatic proxy analysis from higher-resolution terrestrial records at a
97 longer-term timescale, albeit high-resolution stable isotope analyses of
98 foraminifera-dominated tests were recently made across the K/PgB through the main
99 Paleocene (-Eocene) and the orbitally forcing of marine carbon cycles was proposed to
100 interpret the oceanic and climatic conditions and origins (e.g., Coccioni et al., 2012; Hollis et
101 al., 2012; Littler et al., 2014; Zeebe et al., 2017; Barnet et al., 2018, 2019; Gilabert et al.,
102 2021b) and relatively less research of surface ocean with relevant proxies can be also found
103 using planktonic foraminifera (Keller and Lindinger, 1989), nannoplankton (Eldrett et al.,
104 2021), and bulk carbonate (Coccioni et al. 2012; Hull et al., 2020).

105 Stable isotope analysis and estimation of $p\text{CO}_2$ are useful for understanding the driving
106 mechanisms behind changes in paleoclimates and paleoenvironments. These techniques have

107 been widely applied in deep time paleoclimate reconstructions, particularly for greenhouse
108 climates of the Cretaceous–Paleogene. The carbon isotopic composition ($\delta^{13}\text{C}$) of pedogenic
109 carbonate is an important climate proxy for the terrestrial ecosystem and has been adopted to
110 reconstruct $p\text{CO}_2$ (e.g., [Cerling, 1991, 1999](#); [Breecker & Sharp, 2008](#); [Breecker et al., 2009](#)).
111 This proxy has been utilized extensively to calculate $p\text{CO}_2$ during the Cretaceous (e.g., [Lee et
112 al., 1999](#); [Robinson et al., 2002](#); [Sandler, 2006](#); [Huang et al., 2012](#); [Li, X.H. et al., 2014](#); [Li, J.
113 et al., 2016](#); [Harper et al., 2021](#)) and in a short time interval after the K/PgB (e.g., [Nordt et al.,
114 2002, 2003](#); [Huang et al., 2013](#); [Gao et al., 2015, 2021](#); [Zhang et al., 2018](#)). The latter provide
115 some important insights into the driving mechanisms and short-term ($<\sim 500$ Kyr) climate
116 change around the K/PgB. However, few proxies extending to 3–5 Myr interval were reported
117 and applied to analyze terrestrial environment and climate after the K/PgB event.

118 Calcic paleosols are commonly preserved in terrestrial basins, arid zone on the earth (Fig.
119 1). Calcisols are widespread in the Cretaceous basins of South China ([Li et al., 2009](#)) and
120 especially abundant in the Upper Cretaceous sediments of the Nanxiong Basin, where
121 continuous K/PgB successions are exposed (Fig. 2), with good age constraints of
122 biostratigraphy and magnetostratigraphy. Here we use pedogenic carbonate $\delta^{13}\text{C}$ records from
123 the Nanxiong Basin to explore longer-term carbon isotopes and estimate $p\text{CO}_2$ concentration
124 at a higher resolution. We further combine our new results with published data from the
125 Songliao Basin in northeast China and Tornillo Basin (Big Bend National Park), Texas, USA
126 (Fig. 1) to decipher terrestrial responses to the global carbon cycle perturbation in the
127 aftermath of the end-Cretaceous mass extinction.

128

129 **2. Stratigraphy and age constraints**

130 The chronostratigraphy of the uppermost Cretaceous–lowermost Paleocene in the
131 Nanxiong Basin, Guangdong province, South China, has been constructed in a number of
132 biostratigraphy, lithostratigraphy, magnetostratigraphy and stable isotope studies (e.g., [Zhao
133 et al., 1991](#); [Erben et al., 1995](#); [Zhang et al., 2006](#); [Clyde et al., 2010](#); [Li et al., 2010](#); [Tong et
134 al., 2013](#); [Zhang and Li, 2010](#)). In particular, the evolution of mammals and reptiles such as
135 non-avian dinosaurs (e.g., [Zhao et al., 1991, 2009](#); [Clyde et al., 2010](#)), along with the
136 magnetostratigraphy (e.g., [Erben et al., 1995](#); [Clyde et al., 2010](#)), have been primarily used to
137 date the strata. The uppermost Zhutian and Zhenshui formations have been dated as the late
138 Campanian–Maastrichtian, comprising polarity chrons 31R to 29R. The overlying Shanghu
139 Formation (Pingling Member + Xiahui Member) has been dated as the Danian (early
140 Paleocene) in age, comprising polarity chrons from upper 29R to 27R (Fig. 3). The
141 sedimentary sequence of the Datang section has an absolute age range of ~ 9.2 million years,
142 spanning ~ 71.4 – 62.2 Ma based on the International Chronostratigraphic Chart ([Cohen et al.,
143 2013, 2022](#)) and by correlating polarity chrons to absolute age ([Ogg et al., 2012](#);
144 [Vandenbergh et al., 2012](#)). All the beds and thicknesses of the section are adopted from
145 [Zhang et al. \(2006\)](#) in this paper, and those with paleosol horizons span ~ 8.0 (70.0–62.0 Ma)
146 Myr.

147 Well constrained by magnetostratigraphy ([Clyde et al., 2010](#)), the bottom ages of
148 magneto-chrons 31N, 30R, 30N, 29R, 29N, 28R, 28N and 27R are assigned 69.4 Ma, 67.6 Ma,

149 67.4 Ma, 66.6 Ma, 65.7 Ma, 64.9 Ma, 64.6 Ma and 63.5 Ma following the chronostratigraphic
150 chart (Ogg et al., 2012; Vandenberghe et al., 2012), corresponding to the depth of 74.1 m,
151 142.5 m, 234.7 m, 271.3 m, 459.5 m, 492.2 m, 618.0 m and 641.9 m in the Datang section
152 (Zhang et al., 2006), respectively (Fig. 3). These well-dated depths are key for the age
153 determination of calcrete samples, for which interpolation criterion between two neighboring
154 boundary ages was used to constrain the age of individual sample.

155 Nevertheless, a problem involves the placement of the K/PgB within the sedimentary
156 section. As summarized by Zhang et al. (2006), there are about four potential candidates for
157 the placement of the K/PgB. The most popular potential candidates include between Bed 41
158 and 42 or between Bed 42 and 43, based on the disappearance of dinosaur fossils and
159 magnetostratigraphy. Alternatively, the K/PgB could be placed between Bed 48 and 49 based
160 on the first appearance of the mammal genus *Bemalambda*. Zhang and Li (2015) suggest that
161 the entire Pingling Member is of the latest Cretaceous age based on biostratigraphy, although
162 the disappearance of dinosaur fossils occurs in the lowest horizons of this member in their
163 studied sections. By integrating the magnetostratigraphy, disappearance of dinosaur fossils
164 (e.g., Zhang et al., 2006; Clyde et al., 2010) and fluctuations in the Hg/TOC ratio (Zhao et al.,
165 2021), we adopt the K/PgB at the boundary between Bed 42 and Bed 43 in this study. The
166 K/PgB position basically represents the end-Cretaceous mass-extinction even if it is possible
167 that this position could not be precisely followed the original definition K/PgB with the
168 Chicxulub impact time. It is noted that Bed 42 is only 1.7 m thick, whatever the K/PgB is
169 placed between Bed 42 and 43 or Bed 41 and 42 insignificantly influences the deciphering of
170 carbon isotope and $p\text{CO}_2$ trends.

171 In addition, the major part of Bed 21 in the Lower Member of the Zhenshui Formation is
172 covered by farmland. Ma et al. (2018) considered this unexposed section encompassed two
173 polarity chrons (30R and 31N), proposing an alternative of 31R, 32N.1n, and 32N.1r for the
174 underlying Zhutian Formation and an age of 71.5 Ma for the boundary between the Zhenshui
175 and Zhutian formations. As it is not confirmed yet, in this manuscript, we still use the former
176 age classification by Zhang et al. (2006) and Clyde et al. (2010), i.e., Bed 21 encompasses the
177 upper chron 30R.

178 With an uncertainty of ~0.1–0.05 Myr, the age model matches the well-constrained
179 interval within the Songke #1 well in Songliao Basin, northeast China (Gao et al., 2015;
180 Zhang et al., 2018; and references therein) and the Tornillo Basin, USA (e.g., Nordt et al.,
181 2003).

182

183 **3. Materials and methods**

184 3.1. Determination of paleosols

185 There are multiple classifications of paleosols (e.g., Wright, 1992; Mack et al., 1993;
186 Retallack, 2001; Imbellone, 2011), which are mostly based on the US Soil Taxonomy (Soil
187 Survey Staff, 1998). In our study, we use the paleosol classification of Mack et al. (1993) and
188 Retallack (2001).

189 For paleosol determination, detailed field observations were made. We recognized
190 paleosols based on multiple properties and features including 1) color, 2) lithological (fine)
191 texture; 3) soil structure, 4) destratification and horizonation, 5) root traces, 6) particularities
192 of mottles, slickensides, and leaching, 7) composition of B horizon, 8) pedogenic nodules, and
193 9) exposure markers, among other factors.

194 3.2. Diagenetic diagnosis of calcrete samples

195 We used several methods to examine the amount of diagenetic alteration of pedogenic
196 carbonate (calcrete) samples before powder drilling.

197 The field occurrence of calcretes is a relatively direct diagnosis of diagenesis.
198 Petrographic observations of thin-sections under the optical microscope also greatly help to
199 interpret diagenesis. We made thin-sections for most of the samples.

200 Cathodoluminescence (CL) imaging is a common technique for assessing the degree of
201 diagenetic alteration of a carbonate sample. CL imaging is also a common and valid method
202 for examining potential diagenetic modification of pedogenic calcretes. Representative
203 calcrete samples were scanned by a CL electron microscope and imaged. The covariance of
204 carbon and oxygen isotope values can also be used to characterize the extent of diagenetic
205 alteration, in which a high R^2 or R value could indicate significant diagenesis.

206 3.3. Powdering of samples and measurement of carbon-oxygen isotopes

207 Powdered samples of micritic calcites were acquired using a dental drill (aiguille
208 diameter \varnothing 1–2 mm). Drilling was focused on a small point comprising a hard and even
209 calcified area, avoiding any sparry calcite filling cracks, veins, and vugs. 0.2–0.4 mg of
210 powdered sample was prepared for carbon and oxygen isotope analysis. Samples with A and
211 B letters at the end of the numbers represent duplicate samples from the same calcrete to test
212 reproducibility (Table S1). 159 analyses from 96 pedogenic carbonate samples (representing
213 96 corresponding calcisols) were performed, including duplicate analyses for some samples
214 (Table S1 and Fig. 3).

215 The powder was then placed in an oven for drying at 60°C for 10 hours before being
216 moved to the sample vials. Carbon dioxide gas was produced from the sample by adding
217 orthophosphoric acid at 70°C, while isotopic analysis was performed using a DELTA-Plus XP
218 (CFIRMS) mass spectrometer. Analyses were carried out at the State Key Laboratory for
219 Mineral Deposits Research, Nanjing University. Instrument precision was regularly checked
220 using the Chinese national carbonate standard GBW04405 and the international standard
221 NBS19, equating to $\pm 0.1\%$ for $\delta^{13}\text{C}$ and $\delta^{18}\text{O}$ (1σ). Data were calibrated to the international
222 Vienna Pee Dee Belemnite (VPDB) scale using the NBS19 and NBS18 standards.

223

224 3.4. Calculation of $p\text{CO}_2$

225 Reconstructions of $p\text{CO}_2$ from pedogenic carbonate carbon isotope data in deep time
226 (pre-Quaternary) are based on two principal assumptions: 1) soil-respired CO_2 was not

227 produced by C4-plants, and 2) soil CO₂ has a constant carbon isotope composition. The
228 validity of these two assumptions for paleosol records from the pre-Quaternary has been
229 verified (e.g., [Cerling, 1991, 1999](#); [Ekart et al., 1999](#); [Retallack 2001, 2005](#)).

230 An empirical equation for *p*CO₂ concentration has been developed by [Cerling \(1999\)](#) and
231 improved by [Ekart et al. \(1999\)](#):

$$232 \quad C_a = S_{(z)} (\delta^{13}C_s - 1.0044 \delta^{13}C_r - 4.4) / (\delta^{13}C_a - \delta^{13}C_s) \quad [1]$$

233 where *C_a* is the atmospheric *p*CO₂ (ppmV) concentration we are calculating, *S_(z)* is the
234 soil *p*CO₂ concentration (ppmV), and δ¹³C_s, δ¹³C_r, and δ¹³C_a represent the stable carbon
235 isotope compositions of soil *p*CO₂, soil-respired *p*CO₂, and atmospheric *p*CO₂, respectively.

236 In more detail, there are two ways to calculate *C_a*. One way assumes that *S_(z)* is a
237 constant value, while the other assumes that *S_(z)* changes with soil depth. In the second
238 method, *S_(z)* is a function of the thickness of the overburden strata (soil burial depth) to the Bk
239 horizon. This method has been applied to the Quaternary soils (e.g., [Retallack, 2009](#); [Breecker
and Retallack, 2014](#)) and partly to the Cretaceous soils (e.g., [Huang et al., 2013](#); [Gao et al.,
2015](#); [Li et al., 2016](#); [Zhang et al., 2018](#)). However, since it is quite difficult to apply a soil
242 burial depth factor for pre-Cenozoic soils, we used the first method to estimate *C_a* using a
243 constant value for *S_(z)* in this study.

244 Around ten years ago, values of 4000–5000 ppmV were commonly selected for *S_(z)*.
245 However, more and more evidence indicates that *S_(z)* changes with the degree of aridity or
246 humidity, with 1000–1500 ppmV and 2000–2500 ppmV considered to be reasonable values
247 for *S_(z)* in arid to semi-arid soils and semi-arid to semi-humid soils, respectively (e.g., [Brook
et al., 1983](#); [Khadkikar et al., 2000](#); [Breecker et al., 2009, 2010](#)). Therefore, we used a value
249 of *S_(z)* = 2000 ppmV to estimate *p*CO₂ concentrations from pedogenic carbonate in this study,
250 since the Nanxiong, Songliao and Tornillo basins were all located in the northern Hemisphere
251 (semi-) arid zone during the Late Cretaceous and early Paleogene (Fig. 1).

252 δ¹³C_s can be calibrated either with the formula δ¹³C_s = -8.98 + δ¹³C_c ([Ekart et al., 1999](#)),
253 or with δ¹³C_{sc} = (δ¹³C_c + 1000) / ((11.98 - 0.12 * T) / 1000 + 1) - 1000 at 25°C ([Romanek et
al., 1992](#)), where δ¹³C_c is the carbon isotope value of pedogenic carbonate measured in lab.
255 We used the two formula to calibrate the δ¹³C_s in this work, and the results show no distinct
256 differences in the resulting calculated *p*CO₂ concentrations (<10% in error, mostly 3–5%. See
257 Table S1 and S2).

258 δ¹³C_r can often adopt the coeval organic carbon isotope composition (δ¹³C_{om}) of marine
259 and terrestrial sediments. Unfortunately, no high-resolution and high-precision δ¹³C_{om} values
260 are currently available for the late Maastrichtian–early Paleocene. We therefore need to use an
261 alternative approach to calculate δ¹³C_r. Firstly, we can use the transfer function of
262 nannoplankton δ¹³C_m to obtain δ¹³C_a through the equation δ¹³C_a = δ¹³C_m - 7.9 ([Thibault et al.,
2012](#)), in which the isotopic equilibrium fractionation value between ocean and *p*CO₂ was
264 assumed ([Passey and Cerling, 2002](#)). Secondly, the δ¹³C_{om} can be calculated from the equation
265 δ¹³C_a = (δ¹³C_{om} + 18.67) / 1.1 ([Arens et al., 2000](#)). Thirdly, the δ¹³C_r is calculated by
266 subtracting 1‰ from the calculated value of δ¹³C_{om} ([Breecker and Retallack, 2014](#)). We
267 obtained values of three parameters from this process: δ¹³C_{om}, δ¹³C_a, and δ¹³C_r. To calculate

268 these parameters in this study, we chose the nannoplankton $\delta^{13}\text{C}_m$ from the Shearwater SW A9
269 well, central North Sea (Eldrett et al., 2021), which has a relatively complete sequence and
270 high-resolution sampling.

271 All $p\text{CO}_2$ concentration estimates can be found in supplementary Tables S1 and S2 and
272 Fig. 3. It should be noted that we not only calculated new $p\text{CO}_2$ estimates for the latest
273 Cretaceous–early Paleocene pedogenic carbonates from Nanxiong basins, but also
274 recalculated pre-existing estimates from the Songliao Basin, NE China (Gao et al., 2015;
275 Zhang et al., 2018) and Tornillo Basin, USA (Nordt et al., 2003), uniformly using the same
276 process described above.

277 Furthermore, carbon and oxygen isotope data from marine sediments were compiled, and
278 temperatures estimated from oxygen isotope of foraminifera and nannoplankton were
279 recalibrated with refined ages (details see supplementary Text S1 and Table S3).

280

281 4. Results

282 4.1 characteristics of paleosols

283 Field observations show that paleosols are mainly reddish brown, although a few are
284 brownish red and violet red in color, and they were developed in silty/calcareous (occasional
285 gravelly) mudrocks. Calcretes, destratification and slickensides are common in the paleosols,
286 while root traces, mottles and leaching are sometimes associated with mudcracks. Our
287 calcrete samples consisted of hard calcified nodules comprising argillaceous micritic calcite,
288 with a ginger-like, globular, irregular shape and sporadically dispersed occurrence, indicating
289 minimal diagenesis (Fig. 4A and 4B). The observed paleosols are calcisols within the Bk
290 horizon of aridisol and are matured in the IV–VI stage (Machette, 1985).

291 We observed that the calcrete samples comprise argillaceous micritic calcite with a
292 homogeneous texture and composition, lacking any visible carbonate grains or evidence for
293 carbonate replacement and recrystallization. CL images reveal that most of the samples are
294 dull-luminescent and a few are a homogeneous weak orange, verifying a primary origin (Fig.
295 4C and 4D).

296 4.2 Carbon and oxygen isotopes of paleosols

297 Our $\delta^{13}\text{C}$ and $\delta^{18}\text{O}$ values display a very low linear covariance $R^2 = 0.0145$ and a
298 binomial quadratic covariance of $R^2 = 0.0527$ (Fig. 5). The low covariance indicates that $\delta^{13}\text{C}$
299 and $\delta^{18}\text{O}$ values are independent of each other and demonstrates that our calcrete (powder)
300 samples comprise primary carbonate without any significant diagenetic overprint.

301 $\delta^{13}\text{C}$ values range from -12.41‰ to -4.98‰ (mean -8.95‰ , gap $\Delta \approx 6.5\text{‰}$) (Fig. 3 and
302 Table S1), falling the carbon isotope scope of calcisol calcretes. When combined with data
303 from the GCD section, Nanxiong Basin (Clyde et al., 2010), the Songliao Basin (Gao et al.,
304 2015; Zhang et al., 2018) and the Tornillo Basin (Nordt et al., 2003), $\delta^{13}\text{C}$ values encompass a
305 similar range with high-frequency fluctuation (Fig. 6B). Meanwhile, further Kernel
306 smoothing of the composite $\delta^{13}\text{C}$ data exhibits a different scenario with three phases (Fig. 6B):

307 I, decrease with slight decrease spanning 70–66 Ma; II, vibration with great fall and rise
308 spanning 66–63.5 Ma; and III, slight increase spanning 63.5–62.2 Ma.

309 4.3 $p\text{CO}_2$ estimates

310 $p\text{CO}_2$ varies from ~250 ppmV to ~2500 ppmV (mean 960 ppmV, gap $\Delta \approx 2000$ ppmV) in
311 the Nanxiong Basin (Fig. 3 and Table S1). Combined with $p\text{CO}_2$ estimates from the Nanxiong,
312 Songliao and Tornillo basins, recalculated following the methodology employed in this study,
313 $p\text{CO}_2$ ranges between 251 ppmV and 2555 ppmV (mean 1022 ppmV). Within these data, 91.1%
314 (359 of 394 analyses) fall within the 275–1650 ppmV range, 1–6 times the preindustrial level
315 (275 ppmV). As in the $\delta^{13}\text{C}$ record, three corresponding phases of $p\text{CO}_2$ can be differentiated
316 with a minor discrepancy, with slightly rising $p\text{CO}_2$ during phases I and III (Fig. 6C).

317 Using relevant parameters and the formula developed by [Breecker and Retallack \(2014\)](#),
318 uncertainties and Gaussian error (mean, 1σ) are available (Tables S1 and S2 and Fig. 3).
319 Errors (1σ) of $p\text{CO}_2$ range from 85 ppmV to 845 ppmV with a mean 306 ppmV for this work
320 and 332 ppmV for the combined data. Although average uncertainties are a little bit large,
321 ~30–32% for this work and the combined, respectively, within the uncertainty, it is acceptable
322 for trend analysis of $p\text{CO}_2$. The largest source of the uncertainty is caused by the standard
323 error (766 ppmV) of modern soil carbonate ([Breecker and Retallack, 2014](#)). $p\text{CO}_2$ uncertainty
324 will decrease by ~20% if half (383 ppmV) of the standard error is selected, and decrease to
325 ~12% when 1/4 (~191 ppmV) standard error is chosen. Another largest source of error is the
326 $S_{(z)}$ value. $p\text{CO}_2$ will fall from ~31% to ~20% in error if $S_{(z)}=2500$ ppmV is selected instead of
327 2000 ppmV. In addition, the average values of $p\text{CO}_2$ are 719 ppmV, 959 ppmV, and 1199
328 ppmV for the section when $S_{(z)}=1500$ ppmV, 2000 ppmV, 2500 ppmV, respectively, and it will
329 get uncertainties 25% and 17%. More importantly, parameters of temperature, $\delta^{13}\text{C}_r$, $\delta^{13}\text{C}_a$,
330 $\delta^{13}\text{C}_s$, contribute little to the $p\text{CO}_2$ uncertainty, and the tendency of $p\text{CO}_2$ variations is almost
331 same whatever $S(z)$ selection (Fig. 3).

332 Occurrences, compositions, CL images and $\delta^{13}\text{C}$ and $\delta^{18}\text{O}$ value covariances illustrate that
333 calcrete samples have not been significantly altered by diagenesis, and the pedogenic
334 carbonate $\delta^{13}\text{C}$ values are suitable for analyses of carbon cycle and estimated $p\text{CO}_2$.

335

336 5. Discussion

337 5.1. Heavy carbon collapse and recovery linking ecosystem variations

338 Smoothed terrestrial pedogenic $\delta^{13}\text{C}$ records from the combination of Nanxiong Basin
339 and other places display three longer-term phases I, II and III (Fig. 6B) and exhibit a
340 significant longer-term vibration of the main Phase II (66.0–64.5 Ma) with three evolutionary
341 stages (II_a, II_b, and II_c) (Figs. 6 and 7), representing the quick shifts in carbon cycle in the
342 aftermath of the end-Cretaceous extinction.

343 After a moderate increase before the K/PgB, pedogenic carbonate $\delta^{13}\text{C}$ decreases
344 immediately by ~6‰ (from -6.2‰ to -12.2‰) during Stage II_a (~66.0–65.6 Ma), indicating
345 a heavy carbon (^{13}C) collapse (HCC) phase. The coeval HCC is also clear in the marine fine

346 fraction (Keller and Lindinger, 1989), nannoplankton carbonate (Eldrett et al., 2021), benthic
347 foraminifera carbonate (e.g., Hollis et al., 2012; Barnet et al., 2018, 2019) and marine bulk
348 carbonate (Coccioni et al. 2012; Hull et al., 2020), although there could be a little bit age
349 uncertainty (~50 Kyr) for the onset and termination of the HCC phase. It is also distinct that
350 the terrestrial HCC is much larger (~2-3 times) in magnitude than those in marine inorganic
351 and organic $\delta^{13}\text{C}$ (Fig. 7). In addition, a negative excursion of $\delta^{13}\text{C}$ -1.5‰ to -2.8‰ is
352 recorded in the C3 land plants from Western Interior Seaway of North America within ~160
353 Kyr interval after the K/PgB (Arens and Jahren, 2000) .

354 The HCC within ~400 Kyr interval in the early aftermath of the end-Cretaceous
355 extinction is evident from both the marine and terrestrial realms, linking carbon cycle in the
356 surface system reservoir with global ecosystem deterioration. The pertinence of HCC in the
357 two realms is firstly originated from large increase in light carbon preserved in marine
358 sediments and paleosols.

359 In the terrestrial ecosystem, transient carbon and vegetation biomass collapses and
360 recoveries in the order of tens to thousands of years are interpreted as the results of
361 devegetation/deforestation (e.g., Vajda et al., 2001, 2003) or very low primary productivity
362 (Lomax et al., 2004). We herein propose that the devegetation is also responsible for the HCC
363 in a longer-term scale, that is, the devegetation (/deforestation) could have sustained for an
364 interval of ~400 Kyr (the orbital forcing long eccentricity?) lag in the aftermath of the
365 end-Cretaceous extinction, indicating terrestrial ecosystem deterioration while continental
366 weathering had been enhanced (Opdyke and Wilkinson, 1988; Li and Elderfield, 2013).

367 $\delta^{13}\text{C}_s$, the carbon isotope composition of soil $p\text{CO}_2$, determines the $p\text{CO}_2$ estimate while
368 $S_{(z)}$, $\delta^{13}\text{C}_a$ and $\delta^{13}\text{C}_r$ are relatively constant. And $\delta^{13}\text{C}_s$ is further acquired from $\delta^{13}\text{C}_c$, which is
369 derived from carbon isotope compositions of rainfall, soil and pore water, an integrating
370 ecological response to vegetation. When devegetation (/deforestation) takes place, light
371 carbon (^{12}C) from rainfall and atmosphere, has to settle in soil and pore water and record in
372 pedogenic carbonate (calcrete), directly leading to negative $\delta^{13}\text{C}$ excursion.

373 Contemporaneously, the HCC occurs in the marine realm, including those of plankton,
374 benthos and carbonate sediments. This could result from the mass extinction of
375 surface-dwelling plankton and partial collapse of the biological pump or massive export
376 reduction of organic (isotopically light) carbon from the surface to deep ocean, leading to the
377 reduction of the surface-to-deep carbon isotope gradient in the oceans while concentration of
378 light carbon in sea-water and negative $\delta^{13}\text{C}$ (Figs. 6A and 7A). The process could work in
379 same pose with the negative $\delta^{13}\text{C}$ excursion observed in the terrestrial critical zone, while
380 potentially magnifying it within the surface ocean carbon reservoir. Therefore, the ocean
381 carbon cycle appears to couple from atmosphere during the ~400 Kyr interval spanning
382 66.0–65.6 Ma after the K/PgB, despite the different gradients and extents of $\delta^{13}\text{C}$.

383 In early works (1980s-1990s), the carbon cycle marked a decoupling of surface and deep
384 water records, annihilating and sometimes reversing the vertical gradient, i.e. $\delta^{13}\text{C}$ of
385 deep-water benthic foraminifera shows an increase across the K/PgB, while that of planktic
386 foraminifera test and nannofossil record a strong decline, which were accomplished within a
387 transient/moment time interval ($< \sim 100$ Kyr) in geological scale. This paradox was firstly

388 interpreted as the results of a collapse of primary productivity in a lifeless Strangelove Ocean
389 (Alvarez et al., 1980; Hsü and Mackenzie, 1985), and was later modified to represent an
390 incomplete loss of productivity and a strong decline in the biological pump (Living Ocean
391 Model; d'Hondt et al., 1998; Hull and Norris, 2011). Also, other hypotheses were proposed to
392 argue for the contrast carbon cycle and bioevents in marine system, such as Heterogeneous
393 Ocean” (e.g., Hull and Norris, 2011; Alegret et al., 2012; Alegret and Thomas 2013) or
394 geographic heterogeneity (Whittle et al., 2019), methane emission from oceanic slumps
395 (Beerling et al 2002), the effect of extinction of pelagic calcifiers (e.g., D’Hondt and Keller,
396 1991; Bown, 2005), food web collapse (Coccioni and Marsili, 2007), carbonate dissolution
397 (Coccioni et al., 2012; Henehan et al., 2016).

398 The hypothesis of surface water acidification with pH decrease or sulphate-rich vapour
399 has been popularly suggested to be a response to the Chicxulub impact and/or Deccan Trap
400 eruption in moment time (e.g., D’Hondt et al., 1994; Ohno et al., 2014; Tyrrell et al., 2015;
401 Hart et al. , 2019; Henehan et al. 2019) and further modeled and verified (e.g., Henehan et al.
402 2019), consequently leading to the mass extinction across the K/PgB. In deep sea, an enhanced
403 carbonate preservation was observed and attributed to the extinction of pelagic calcifiers that
404 caused carbonate oversaturation of the oceans (see e.g. Alegret & Thomas 2013; Henehan et
405 al., 2019). Similarly, the release of methane hydrates (Beerling et al 2002) is not supported by
406 the lack of a significant negative carbon isotope excursion within deep sea carbonates of this
407 time and the quick methane oxidization would have resulted in expected $p\text{CO}_2$ increase that
408 was not observed in the reconstruction data.

409 Above hypotheses indicate an instability of marine environment (e.g., Coccioni and
410 Marsili, 2007; Sinnesael et al., 2016; Gilabert et al., 2021) and terrestrial system (e.g., Vajda
411 et al., 2001, 2003; Vajda and McLoughlin, 2007; Gertsch, et al., 2011; Spicer and Collinson,
412 2014; Donovan et al., 2020), and have been linked to the Chicxulub impact and / or Deccan
413 Trap eruption (e.g., Gertsch, et al., 2011; Keller, 2014; Barnet, et al., 2018; Zhang et al., 2018;
414 Henehan et al., 2019) although there are some oppositional evidence (e.g., Dzombak et al.,
415 2020; Percival et al., 2018; Milligan et al., 2019). However, the instability (collapse) and rapid
416 recovery of ecology and environment took place instantaneously soon after the eruption and
417 impact events, and finished in a geological ultra short-term ($< \sim 1.0$ Kyr) interval (e.g.,
418 Coccioni and Marsili, 2007; Gertsch et al., 2011; Woelders et al., 2017; Gilabert et al., 2021).
419 These hypotheses may not be eligible for the HCC in a longer term ($> \sim 100$ Kyr) duration.
420 Namely, the role of the Chicxulub impact and / or Deccan Trap eruption to the HCCs with ~ 400
421 Kyr duration of both global marine and terrestrial systems remains suspected. At least the
422 consecutive great decrease in marine and terrestrial $\delta^{13}\text{C}$ is not compatible with the fading
423 pulse eruption (vacancy between 65.85–65.65 Ma) of the Deccan Traps (Fig. 7E. Schoene et
424 al., 2019, 2021).

425 In Stage II_b, the $\delta^{13}\text{C}$ values show a smoothing variation at a lowest level of (surface sea)
426 marine fine fraction ca. -1.5‰ (Keller and Lindinger, 1989), marine bulk carbonate $\sim -1.5\text{‰}$
427 (Coccioni et al., 2012) and terrestrial pedogenic carbonate ca. -12‰ , spanning ~ 300 Kyr
428 (~ 65.6 – 65.3 Ma). The onset of Stage II_b, also the final of Stage II_a, seems coincident with the
429 cessation of Deccan Traps volcanism, implying the termination of eruptional gas contribution.
430 Thus, a significant positive excursion of carbon isotope would be expected. Nevertheless, we

431 do not see such a distinct shift in our terrestrial $\delta^{13}\text{C}$ record, and so not in the marine
432 counterpart (Fig. 7A and 7B). The regime of (~300 Kyr duration) sustaining lowest $\delta^{13}\text{C}$ could
433 be the feedback to the termination of the previous (66.0–65.6 Ma) severe environmental
434 perturbations for a requirement of global stabilization system, before the rapid recovery in the
435 coming stage (II_c), likely corresponding to the DAN-C2 event of carbon redistribution
436 (Quillévére et al., 2008). The exception of distinct positive shift at ~65.5 Ma, correlatable
437 between marine and terrestrial system (Fig. 7) is suggested an adjustment for the ecosystem
438 stabilization, or an response to a geologic event at the sharp time, perhaps the ALE volcanic
439 ash (Odin et al., 1992).

440 With the termination of HCC (Fig. 7), $\delta^{13}\text{C}$ value quickly increases in a ~800 Kyr span
441 (Fig. 7A and 7B): pedogenic carbonate from ca. -12.0‰ to ca. -6.5‰, marine fine fraction
442 from ca. -1.5‰ to 1.0‰ (Keller and Lindinger, 1989), marine bulk carbonate from ~1.0‰ to
443 2.5‰ (Coccioni et al., 2012) although there is a little bit uncertainty when $\delta^{13}\text{C}$ reaches the
444 pre-K/PgB level. The rapid rebound of carbon isotope indicates the recovery process is
445 closely coherent in both surface marine and terrestrial realms during the interval of
446 ~65.3–64.5 Ma (Phase II_c).

447 Overall, the pattern of collapse, smooth and rebound process of $\delta^{13}\text{C}$ values is quite
448 similar in both surface sea and terrestrial system, suggesting global changes of marine and
449 terrestrial ecosystem and environment. This process is approximately close to those of initial
450 marine biotic shift in abundance and taxonomic richness of benthic molluscan faunas in
451 Antarctica with ~0.32 Myr and ~1.00 Myr period after the K/PgB (Whittle, 2019),
452 respectively.

453 Surprisingly, $\delta^{13}\text{C}$ of benthic foraminifera continuously decreases with a higher extent till
454 65.2 Ma (Barnet et al., 2018; Norouzi et al., 2021), similar to the framework of the Kernel
455 smoothed curve of the pedogenic carbonate $\delta^{13}\text{C}$ (comp. Fig. 6A and 6B), whereas quite
456 different from the pedogenic $\delta^{13}\text{C}$ pattern in Stage II_b and II_c (comp. Figs. 7 and 6). And the
457 trend of terrestrial $\delta^{13}\text{C}$ also contrast strongly with the slight decrease in deep sea benthic $\delta^{13}\text{C}$
458 after ~65.2 Ma (Barnet et al., 2018). As a whole, $\delta^{13}\text{C}$ exhibits variation within the terrestrial
459 realm and surface ocean during the early Paleocene, but display slight change within the deep
460 South Atlantic Ocean (Barnet et al., 2018, 2019).

461 These discrepancies could result from different ecosystem conditions in water
462 temperature, productivity, nutrition, photosynthesis, etc., where devegetation caused
463 productivity decrease and heavy carbon loss in critical zone and biological pump fading or
464 fail of led to massive export reduction of organic light carbon from surface sea to deep ocean.
465 Therefore, the deep ocean carbon cycle appears to have become decoupled from the surface
466 ocean and atmosphere during the 3 Myr interval spanning 65.3–62.3 Ma in the aftermath of
467 the end-Cretaceous extinction.

468 5.2. Variations of $p\text{CO}_2$ concentration documenting vibrant climate change

469 Within the age uncertainties, the estimated $p\text{CO}_2$ shows a quite similar style with the
470 pedogenic carbonate $\delta^{13}\text{C}$ (Figs 6 and 7). Three phases can be also recognized, in which four
471 stages are further subdivided for Phase II, with a high degree of variations.

472 During Stage II_a, $p\text{CO}_2$ steeply declines by ~2000 ppmV (~2500–250 ppmV) spanning
473 ~400 Kyr after a high increase (~800 ppmV) of the pre-K/PgB. This rapid $p\text{CO}_2$ fall was not
474 observed in the Tornillo Basin in North America (Nordt et al., 2003), when the data are
475 calibrated to our age model (Table S2), where biochemical behaviors do not reveal
476 demonstrable changes in soil characteristics (Nordt et al., 2011).

477 The significant decrease in $p\text{CO}_2$ with albeit six to seven times that of pre-industrial
478 values would expect to have resulted in the coeval global cooling. The mean annual
479 temperature fall ~4°C (Dworkin et al., 2005) supports this cooling tendency on land. Despite
480 this apparent marked decrease in $p\text{CO}_2$, coeval SST (surface sea temperature) fluctuates
481 significantly (Keller and Lindinger, 1989) and exhibit a distinct decrease by ~8°C (32°C to
482 26°C; Fig. 7D) when use the Kernel smoothed data with the calibrations of age and
483 parameters (Supplementary Text S1 and Table S3). The trend similarity between $p\text{CO}_2$ and
484 SST indicate a rapid climate deterioration commenced shortly after the K/PgB in both the
485 terrestrial realm and surface ocean.

486 Regardless of the precise age correlation, great falls of $p\text{CO}_2$ and coeval SST would be
487 responses to the cooling, which highly resulted in productivity reduction and devegetation as
488 well as $\delta^{13}\text{C}$ negative shift in surface ocean and subaerial systems. During Stage II_a, the
489 Deccan volcanic eruption would instigate an increase in $p\text{CO}_2$ and climatic warming even
490 though only 25% of the Deccan Traps volume in the period (Sprain et al., 2019, 2021), that
491 means $p\text{CO}_2$ and coeval SST would have had a great rise with permanent $\delta^{13}\text{C}$ positive shift.
492 The decoupling of climatic proxies from expected effects by volcanic eruption suggests the
493 Deccan Trap volcanism may have not contributed much to the climate change after the
494 Chicxulub impact in a longer-term interval (~400 Kyr soon after the K/PgB). Then, would the
495 bolide impact be responsible for the secular fall of $p\text{CO}_2$ and coeval SST? Our answer is
496 negative.

497 Following the Chicxulub impact, the absolute abundance of benthic foraminifera
498 increased (Arreguín-Rodríguez et al., 2021) and bottom water temperature (BWT) rose by ~3°C
499 in the tropical Pacific and by 1.5–2°C in the South Atlantic (Jung et al., 2013; Barnet et al.,
500 2018), while SST oscillated between 23–34°C in the south-western Tethys (Keller and
501 Lindinger, 1989). More importantly, dust clouds and possible sulfate aerosols resulting in the
502 impact winter would only circulate within the atmosphere for an extremely short duration,
503 with estimates ranging from less than ten years (Kring, 2003) to millennia at most (Galeotti et
504 al., 2004). These findings suggest that bolide impact exerted a heterogeneous impact on
505 global climate change in an instantaneous time gap, therefore could not have played a causal
506 role in a longer-term (> ~100 Kyr) duration climate change after the K/PgB (Keller et al.,
507 2016). However, it is likely to have played a vital role in destroying the habitats of organisms
508 and perturbing the very short-term carbon cycle in the immediate aftermath of the K/PgB.

509 In the span of ~65.6–65.3 Ma (Stage II_b), $p\text{CO}_2$ remains at relatively low values of
510 ~250–500 ppmV (Fig. 7B), comparable to those of today, indicating a persistently cool (or
511 even cold) climatic regime. In the deep sea, benthic foraminifera test $\delta^{13}\text{C}$ and BWT remain
512 fairly stable without significant change (Fig. 6A and 6D). This roughly happens to the SST in
513 the southern West Tethys (Keller et al., 2016), where SST mainly is stable at 24–26°C with an

514 exception of abrupt rising to $\sim 34^{\circ}\text{C}$ at ~ 65.5 Ma (Fig. 7D). The exceptional high SST value is
515 similar with the $\delta^{13}\text{C}$ in marine and terrestrial realms, which might be originated by geological
516 event, perhaps the ALE volcanic event (Odin et al., 1992). It is noted that the lowest $p\text{CO}_2$ is
517 often higher than the preindustrial 275 ppmV. Even though 250–275 ppmV can be seen at
518 several intermittences (Fig. 7C), each does not persist for ~ 100 Kyr, which could not have
519 driven ice cap formation in polar regions.

520 $p\text{CO}_2$ concentration quickly rose by 1400 ppmV (from ~ 250 ppmV to 1650 ppmV) in
521 ~ 800 Kyr interval (Fig. 7C), likely indicating rapid warming during the interval of ~ 65.3 – 64.5
522 Ma (Phase II_c). The SST rises by $\sim 7^{\circ}\text{C}$ (23°C to 30°C) (Keller and Lindinger, 1989), showing
523 a rough comparison although uncertainties occur at some age variation boundaries between
524 the two proxies.

525 Overall, the post-K/PgB longer-term trend of terrestrial climate cycles is closely
526 comparable to coeval changes of SST estimated from $\delta^{18}\text{O}$ values of planktonic foraminifera
527 (Jung et al., 2013) and TEX_{86} (Vellekoop et al., 2016; Woelders et al., 2017), and to the
528 Maastrichtian BWT estimated from benthic foraminifera $\delta^{18}\text{O}$ data (e.g., Hollis et al., 2012;
529 Barnet et al., 2018, 2019). The similarity between the $p\text{CO}_2$ trend, SST and BWT indicates
530 that consistent longer-term global climate change occurred in both terrestrial and surface
531 ocean environments during the early Paleocene.

532 However, BWT appears to become decoupled the deep ocean temperature from surface
533 ocean and terrestrial realms during Phase II and III. That is the post-K/PgB vibration in $p\text{CO}_2$
534 and SST are accompanied by a coeval longer-term rise in BWT in the aftermath of the
535 end-Cretaceous extinction till 62.5 Ma (Fig. 6D), representing a major decoupling between
536 the surface and deep ocean during times of rapid but transient climate change, $p\text{CO}_2$ turnover
537 and volcanic pulse. As discussed before, the release of significant quantities of sulfate
538 aerosols during Deccan Traps outgassing may be sufficient to counteract the warming effects
539 of rising $p\text{CO}_2$, with a potential decrease of global surface temperature by $\sim 4.5^{\circ}\text{C}$ from a
540 single pulse of decade-long Deccan Traps eruptions (Schmidt et al., 2016), but such a cooling
541 effect would only be short-term and would not affect longer-term climatic evolution due to the
542 extremely short residence time (~ 50 years) of sulfate aerosols in the atmosphere (Kring, 2003;
543 Galeotti et al., 2004; Schmidt et al., 2016). The sulfate aerosols would be then considered as
544 instantaneous in terms of geological time and are almost impossible to be preserved or
545 recognized in the geological record. Such extremely short-lived events are unlikely to be
546 recorded even in high-resolution paleothermometry studies, where decadal-centennial
547 sampling is extremely difficult to make (Schmidt et al., 2016; Bond and Sun, 2021).
548 Accordingly, the bolide impact winter would have led to an instantaneous cooling. Therefore,
549 we suggest that Deccan Traps volcanism and Chicxulub impact perturbed global climate
550 immediately after the K/PgB), but did not have a significant effect on longer-term climate.
551 That is to say, they would not be the key factors that caused the longer-term vibration in
552 $p\text{CO}_2$ and SST and secular rise in BWT in the aftermath of the end-Cretaceous extinction.

553 Integrating the evolution of terrestrial $\delta^{13}\text{C}$ and $p\text{CO}_2$ with marine $\delta^{13}\text{C}$, BWT and SST,
554 we propose that the climate and environment have a rapidly and vibrantly change during the
555 interval of ~ 1.5 Myr (66.0–64.5 Ma) after the end-Cretaceous mass-extinction. Proxies of

556 carbon isotope, $p\text{CO}_2$ and SST show a pattern of dramatic reduction, short smooth towards
557 rapid rebound, unraveling a process of deterioration, stabilization and recovery for the
558 longer-term global ecosystem and climate, likely representing the response to carbon cycle
559 perturbation.

560 It is proposed that the ecosystem recovery was fast, erratic and unstable in the terrestrial
561 and surface ocean ecosystems, but slow and stable in the deep sea. Alternatively, climate and
562 environmental perturbation may have been much more significant in the surface ocean and
563 terrestrial realm than in the deep sea, resulting in a relatively shorter and faster ecosystem
564 recovery than expected in surface realms (e.g., ~1–2 Myr, [Dessert et al., 2001](#); [Donovan et al., 2016](#);
565 or >3 Myr, [D'Hondt et al., 1998](#); [Adams and Mann, 2004](#)). This may imply that the
566 terrestrial and surface ocean realms were much more sensitive to climatic changes after the
567 K/PgB than the deep ocean, which may have been relatively buffered due to the time lag for
568 such major temperature changes to infiltrate into the deep sea; and the recovery capability of
569 terrestrial ecosystems could be much more powerful than we expect ([Keller et al., 2016](#)). The
570 changes in earth system processes likely correlating with patterns of pedogenic and marine
571 fossil-test carbonate $\delta^{13}\text{C}$ values, $p\text{CO}_2$, and sea-water temperatures, suggest frameworks of
572 feedback pathways are responsible for the comparable longer-term carbon cycle and
573 temperature tendency in both terrestrial and marine ecosystems at the time.

574 Causal changes in the longer-term carbon cycle and climate invoke exchanges of carbon
575 between Earth's crust, ocean, atmosphere and biosphere, involving complex processes of
576 carbon burial, volcanism, weathering, organic matter oxidation, nutrient cycling, atmospheric
577 CO_2 and O_2 ([Berner, 2003](#)), and others. When examining these processes prior to the K/PgB,
578 fluctuations over timescales on the order of ~10 Myr in the relative rate of organic carbon
579 burial and oxygen production ([Berner, 2001, 2003; 2009](#)), carbonate precipitation ([Opdyke
580 and Wilkinson, 1988; Li and Elderfield, 2013](#)), island basalt and continental silicate
581 weathering ([Li and Elderfield, 2013](#)), and oceanic ridge spreading ([Muller et al., 2008](#)) have
582 been shown by modelling experiments. Following the K/PgB, long scale cycles were actually
583 observed on the order of ~3–4 Myr in the relative rate of organic carbon burial ([Berner, 2003](#)),
584 carbonate sedimentation ([Opdyke and Wilkinson, 1988; Li and Elderfield, 2013](#)), and
585 continental sediment weathering ([Li and Elderfield, 2013](#)), which may not play key roles on
586 the longer-term (~100–1000 Kyr) vibration of ecosystem and climate in the early aftermath of
587 the end-Cretaceous extinction.

588

589 **Conclusions**

590 This study has expanded on the previous studies focused on pedogenic carbonate stable
591 isotope and atmospheric CO_2 across the K/Pg boundary. New data and compiles show a
592 similar vibration pattern of $\delta^{13}\text{C}$ in pedogenic and marine carbonates and of the reconstructed
593 $p\text{CO}_2$ and SST with decoupling BWT.

594 Looking in more detail, three evolutionary phases (I–III) of carbon cycle and $p\text{CO}_2$ are
595 distinguished: Phase I (70.0–66.0 Ma), II (66.0–63.5 Ma), III (63.5–62.3 Ma), and four stages
596 (II_a–II_d) are further subdivided in Phase II, representing the key period of the climate and
597 environment perturbation in the aftermath of the end-Cretaceous extinction. In the earliest

598 stage (II_a, 66.0–65.6 Ma), terrestrial $\delta^{13}\text{C}$ values greatly decline (HCC) and $p\text{CO}_2$ rapidly fall,
599 accompanied by significant changes in ecosystem and climate. The two proxies are relatively
600 constant for ~ 300 Kyr (II_b, 65.6–65.3 Ma) since then. Rebounding of $\delta^{13}\text{C}$ and $p\text{CO}_2$ quickly
601 finishes to the pre-K/PgB levels in a span ~ 800 Kyr (II_c, 65.3–62.5 Ma). The pattern of $\delta^{13}\text{C}$
602 and $p\text{CO}_2$ change reveals a vibrant process of deterioration, stabilization and recovery for the
603 longer-term terrestrial ecosystem and environment, spanning ~ 1.5 Myr (66.0–64.5 Ma).

604 With comparison to the compiled marine records, $\delta^{13}\text{C}$ values of surface sea sediments
605 (fine fraction, nannoplankton, benthic foraminifera and marine bulk carbonate) and SST show
606 a quite similar pattern of the pedogenic $\delta^{13}\text{C}$ and $p\text{CO}_2$. However, $\delta^{13}\text{C}$ and BWT of benthic
607 foraminifera decouple the proxies in the surface ocean and terrestrial realms. That is, the
608 post-K/PgB variation in surface ocean and terrestrial $\delta^{13}\text{C}$, SST and $p\text{CO}_2$ is accompanied by
609 a coeval longer-term decrease $\delta^{13}\text{C}$ and secular rise in BWT in deep ocean, representing a
610 major decoupling between the surface system and deep ocean during times of ecosystem and
611 climate changes. Together, these proxy changes suggest that the terrestrial and surface ocean
612 ecosystems and climates experienced an unstable, much more unpredictable and erratic
613 recovery process than the deep ocean in the aftermath of the end-Cretaceous extinction.

614 Besides triggering in the end-Cretaceous extinction, Deccan Traps volcanism and
615 Chicxulub impact perturbed global instantaneous environment and climate immediately after
616 the K/PgB, in extremely short time ($< \sim 1.0$ Kyr), leading to transient collapse of primary
617 productivity, surface water acidification, release of methane hydrate, etc.; but did not have a
618 significant effect on longer-term ($> \sim 100$ Kyr) climate. Namely, the two events would not be
619 the key factors that caused the longer-term vibration in $\delta^{13}\text{C}$, $p\text{CO}_2$ and SST as well as secular
620 rise in BWT in the aftermath of the end-Cretaceous extinction. In particular, the HCC and
621 $p\text{CO}_2$ fall after the K/PgB is at odds with the expected positive shift and rise in $p\text{CO}_2$
622 following the Deccan Traps and Chicxulub impact.

623

624 **Acknowledgements**

625 We thank the reviewers for their helpful comments and constructive suggestions. Dr.
626 James. Barnet is grateful for the revision of some key knowledge and language polishment in
627 the early version of the manuscript. Dr. Yuan Gao helps make the Kernel smoothing of data,
628 Mr Yong Zhou took part in the field work in early time. It is acknowledged this research was
629 supported by the National Natural Science Foundation of China (NSFC grants 42172106 and
630 41372016).

631 The supporting information files (Text S1 and Tables S1–S3) are deposited and can be
632 found in the repository of Figshare (<https://figshare.com/s/a75143bb6874e231d82c>) or DOI:
633 10.6084/m9.figshare.19649739 when this article is accepted for publication.

634

635 **References**

636 Adams, J. B., Mann, M. E., & D'Hondt, S. (2004). The Cretaceous-Tertiary extinction:
637 Modeling carbon flux and ecological response. *Paleoceanography*, 19, PA1002.

638 <https://doi.org/10.1029/2002PA000849>.

639 Alegret, L., & Thomas, E. (2013). Benthic foraminifera across the Cretaceous/Paleogene
640 boundary in the Southern Ocean (ODP Site 690): Diversity, food and carbonate
641 saturation. *Marine Micropaleontology*, *105*, 40–51.

642 Alegret, L., Thomas, E., & Lohmann, K. C. (2012). End-Cretaceous marine mass extinction
643 not caused by productivity collapse. *Proceedings of the National Academy of Sciences*,
644 *109*(3), 728–732. <https://doi.org/10.1073/pnas.1110601109>

645 Alvarez, L. W., Alvarez, W., Asaro, F., & Michel, H. V. (1980). Extraterrestrial Cause for the
646 Cretaceous-Tertiary Extinction - Experimental Results and Theoretical Interpretation.
647 *Science*, *208*(4448), 1095–1108. <https://doi.org/10.1126/science.208.4448.1095>.

648 Arens, N. C., & Jahren, A. H. (2000). Carbon isotope excursion in atmospheric CO₂ at the
649 Cretaceous-Tertiary boundary: Evidence from terrestrial sediments. *Palaios*, *15*(4),
650 314–322. <https://doi.org/10.2307/3515539>

651 Arens, N. C., Jahren, A. H., & Amundson, R. (2000). Can C3 plants faithfully record the
652 carbon isotopic composition of atmospheric carbon dioxide? *Paleobiology*, *26*(1),
653 37-164.

654 Arreguín-Rodríguez, G. J., Barnet, J. S. K., Leng, M. J., Littler, K., Kroon, D., Schmidt, D. N.,
655 Thomas, E., & Alegret, L. (2021). Benthic foraminiferal turnover across the Dan-C2
656 event in the eastern South Atlantic Ocean (ODP Site 1262). *Palaeogeography*,
657 *Palaeoclimatology*, *Palaeoecology*, *572*, 110410.
658 <https://doi.org/10.1016/j.palaeo.2021.110410>

659 Barnet, J. S. K., Littler, K., Kroon, D., Leng, M. J., Westerhold, T., Röhl, U., & Zachos, J. C.
660 (2018). A new high-resolution chronology for the late Maastrichtian warming event:
661 Establishing robust temporal links with the onset of Deccan volcanism. *Geology*,
662 *46*(2), 147-150. <https://doi.org/10.1130/G39771.1>

663 Barnet, J. S. K., Littler, K., Westerhold, T., Kroon, D., Leng, M. J., Bailey, I., Röhl, U., &
664 Zachos, J. C. (2019). A High-Fidelity Benthic Stable Isotope Record of Late
665 Cretaceous–Early Eocene Climate Change and Carbon-Cycling. *Paleoceanography*
666 *and Paleoclimatology*, *34*(4), 672–691. <https://doi.org/10.1029/2019PA003556>

667 Beerling, D. J., Lomax, B. H., Royer, D. L., Upchurch, G. R., & Kump, L. R. (2002). An
668 atmospheric pCO₂ reconstruction across the Cretaceous-Tertiary boundary from leaf
669 megadossils. *Proceedings of the National Academy of Sciences*, *99*(12), 7836–7840.

670 Berner, R. A. (2001). Modelling atmospheric O₂ over Phanerozoic time. *Geochimica et*
671 *Cosmochimica Acta*, *65*, 685-694

672 Berner, R. A. (2003). The long-term carbon cycle, fossil fuels and atmospheric composition.
673 *Nature*, *426*(6964), 323–326. <https://doi.org/10.1038/nature02131>

674 Berner, R. A. (2009). Phanerozoic atmospheric oxygen: new results using the
675 GEOCARBSULF model. *American Journal of Science*, *309*, 603–606.
676 <https://doi.org/doi:10.2475/07.2009.03>

677 Bond, D. P. G., & Sun, Y. D. (2021). Global Warming and Mass Extinctions Associated With
678 Large Igneous Province Volcanism. In R. E. Ernst, A. J. Dickson, & A. Bekker (Eds.),
679 *Large Igneous Provinces: A Driver of Global Environmental and Biotic Changes* (pp.
680 85–102): Geophysical Monograph Series.

681 Boucot, A. J., Chen, X., Scotese, C. R., & Morley, R. J. (Cartographer). (2013). Phanerozoic

682 Paleoclimate: An Atlas of Lithologic Indicators of Climate

683 Bown, P. (2005). Selective calcareous nannoplankton survivorship at the Cretaceous-Tertiary
684 boundary. *Geology*, 33, 653–656.

685 Breecker, D. O., & Retallack, G. (2014). Refining the pedogenic carbonate atmospheric CO₂
686 proxy and application to Miocene CO₂. *Palaeogeography, Palaeoclimatology,*
687 *Palaeoecology*, 406, 1–8. <https://doi.org/10.1016/j.palaeo.2014.04.012>

688 Breecker, D. O., & Sharp, Z. D. (2008). A field and laboratory method for monitoring the
689 concentration and isotopic composition of soil CO₂. *Rapid Communications in Mass*
690 *Spectrometry*, 22(4), 449–454. <https://doi.org/10.1002/rcm.3382>

691 Breecker, D. O., Sharp, Z. D., & McFadden, L. D. (2009). Seasonal bias in the formation and
692 stable isotope composition of pedogenic carbonate in modern soil from central New
693 Mexico, USA. *Geological Society of America Bulletin*, 121, 630–640.

694 Breecker, D. O., Sharp, Z. D., & McFadden, L. D. (2010). Atmospheric CO₂ concentrations
695 during ancient greenhouse climates were similar to those predicted for AD 2100.
696 *Proceedings of the National Academy of Sciences of the United States of America*,
697 107(2), 576–580. <https://doi.org/10.1073/pnas.0902323106>

698 Brook, G. A., Folkoff, M. E., & Box, E. O. (1983). A World Model of Soil Carbon-Dioxide.
699 *Earth Surface Processes and Landforms*, 8(1), 79–88.
700 <https://doi.org/10.1002/esp.3290080108>

701 Cerling, T. E. (1991). Carbon dioxide in the atmosphere; evidence from Cenozoic and
702 Mesozoic Paleosols. *American Journal of Science*, 291(4), 377–400.
703 <https://doi.org/10.2475/ajs.291.4.377>

704 Cerling, T. E. (1999). Stable Carbon Isotopes in Palaeosol Carbonates. In M. Thiry & R.
705 Simon-Coincon (Eds.), *Palaeoweathering, palaeosurfaces and related continental*
706 *deposits* (Vol. 27, pp. 43–60): Blackwell, Oxford, International.

707 Clyde, W. C., Ting, S. Y., Snell, K. E., Bowen, G. J., Tong, Y. S., Koch, P. L., Li, Q., &
708 Wang, Y. Q. (2010). New Paleomagnetic and Stable-Isotope Results from the
709 Nanxiong Basin, China: Implications for the K/T Boundary and the Timing of
710 Paleocene Mammalian Turnover. *Journal of Geology*, 118(2), 131–143.
711 <https://doi.org/10.1086/649893>

712 Coccioni, R., Bancalà, G., Catanzariti, R., Fornaciari, E., Frontalini, F., Giusberti, L., Jovane,
713 L., Luciani, V., et al. (2012). An integrated stratigraphic record of the Palaeocene–
714 lower Eocene at Gubbio (Italy): New insights into the early Palaeogene hyperthermals
715 and carbon isotope excursions. *Terra Nova*, 24, 380–386.
716 <https://doi.org/10.1111/j.1365-3121.2012.01076.x>

717 Coccioni, R., & Marsili, A. (2007). The response of benthic foraminifera to the K–Pg
718 boundary biotic crisis at Elles (northwestern Tunisia). *Palaeogeography,*
719 *Palaeoclimatology, Palaeoecology*, 255(1–2), 157–180.
720 <https://doi.org/10.1016/j.palaeo.2007.02.046>

721 Cohen, K. M., Finney, S. C., Gibbard, P. L., & Fan, J. X. (2013). The ICS International
722 Chronostratigraphic Chart 36, 199–204.

723 Cohen, K. M., Harper, D. A. T., Gibbard, P. L., & Fan, J. X. (2022). International
724 Chronostratigraphic Chart. In: International Commission on Stratigraphy.

725 D’Hondt, S., & Keller, G. (1991). Some patterns of planktic foraminiferal assemblage

726 turnover at the Cretaceous-Tertiary boundary. *Marine Micropaleontology*, 17, 77–118.

727 D'Hondt, S., Pilson, M. E. Q., Sigurdsson, H., Hanson, A. K., & Carey, S. (1994).

728 Surface-water acidification and extinction at the Cretaceous-Tertiary boundary.

729 *Geology*, 22, 983–986.

730 Dessert, C., Dupre, B., Francois, L. M., Schott, J., Gaillardet, J., Chakrapani, G., & Bajpai, S.

731 (2001). Erosion of Deccan Traps determined by river geochemistry: impact on the

732 global climate and the Sr⁸⁷/Sr⁸⁶ ratio of seawater. *Earth and Planetary Science Letters*,

733 188(3–4), 459–474. [https://doi.org/10.1016/S0012-821x\(01\)00317-X](https://doi.org/10.1016/S0012-821x(01)00317-X)

734 D'Hondt, S., Donaghay, P., Zachos, J. C., Luttenberg, D., & Lindinger, M. (1998). Organic

735 carbon fluxes and ecological recovery from the Cretaceous-Tertiary mass extinction.

736 *Science*, 282(5387), 276–279. <https://doi.org/10.1126/science.282.5387.276>

737 Donovan, M. P., Iglesias, A., Wilf, P., Labandeira, C. C., & Cúneo, N. R. (2016). Rapid

738 recovery of Patagonian plant–insect associations after the end-Cretaceous extinction.

739 *Nature Ecology & Evolution*, 1(1), 0012. <https://doi.org/10.1038/s41559-016-0012>

740 Dworkin, S. I., Nordt, L., & Atchley, S. (2005). Determining terrestrial paleotemperatures

741 using the oxygen isotopic composition of pedogenic carbonate. *Earth and Planetary*

742 *Science Letters*, 237(1–2), 56–68. <https://doi.org/10.1016/j.epsl.2005.06.054>

743 Dzombak, R. M., Sheldon, N. D., Mohabey, D. M., & Samant, B. (2020). Stable climate in

744 India during Deccan volcanism suggests limited influence on K–Pg extinction.

745 *Gondwana Research*, 85, 19–31. <https://doi.org/10.1016/j.gr.2020.04.007>

746 Ekart, D. D., Cerling, T. E., Montanez, I. P., & Tabor, N. J. (1999). A 400 million year carbon

747 isotope record of pedogenic carbonate: Implications for paleoatmospheric carbon

748 dioxide. *American Journal of Science*, 299(10), 805–827.

749 <https://doi.org/10.2475/ajs.299.10.805>

750 Eldrett, J. S., Vieira, M., Gallagher, L., Hampton, M., Blaauw, M., & Swart, P. K. (2021).

751 Late Cretaceous to Palaeogene carbon isotope, calcareous nannofossil and

752 foraminifera stratigraphy of the Chalk Group, Central North Sea. *Marine and*

753 *Petroleum Geology*, 124, 104789. <https://doi.org/10.1016/j.marpetgeo.2020.104789>

754 Erben, H. K., Ashraf, A. R., Böhm, H., Hahn, G., Hambach, U., Krumsiek, K., Stets, J., Thein,

755 J., et al. (1995). Die Kreide/Tertiär-Grenze im Nanxiong-Becken (Kontinentalfazies,

756 Südostchina). *Erdwissenschaftliche Forschung*, 32, 1–245.

757 Galeotti, S., Brinkhuis, H., & Huber, M. (2004). Records of post–Cretaceous-Tertiary

758 boundary millennial-scale cooling from the western Tethys: A smoking gun for the

759 impact-winter hypothesis? *Geology*, 32(6). <https://doi.org/doi:10.1130/G20439.1>

760 Gao, Y., Ibarra, D. E., Caves Rugenstein, J. K., Chen, J. Q., Kukla, T., Methner, K., Gao, Y. f.,

761 Huang, H. Y., et al. (2021). Terrestrial climate in mid-latitude East Asia from the

762 latest Cretaceous to the earliest Paleogene: A multiproxy record from the Songliao

763 Basin in northeastern China. *Earth-Science Reviews*, 216, 103572.

764 <https://doi.org/10.1016/j.earscirev.2021.103572>

765 Gao, Y., Ibarra, D. E., Wang, C. S., Caves, J. K., Chamberlain, C. P., Graham, S. A., & Wu,

766 H. S. (2015). Mid-latitude terrestrial climate of East Asia linked to global climate in

767 the Late Cretaceous. *Geology*, 43(4), 287–290. <https://doi.org/10.1130/G36427.1>

768 Gertsch, B., Keller, G., Adatte, T., Garg, R., Prasad, V., Berner, Z., & Fleitmann, D. (2011).

769 Environmental effects of Deccan volcanism across the Cretaceous-Tertiary transition

770 in Meghalaya, India. *Earth and Planetary Science Letters*, 310, 272–285.

771 Gilabert, V., Arenillas, I., Arz, J. A., Batenburg, S. J., & Robinson, S. A. (2021a). .
772 Multiproxy analysis of paleoenvironmental, paleoclimatic and paleoceanographic
773 changes during the early Danian in the Caravaca section (Spain). *Palaeogeography,*
774 *Palaeoclimatology,* *Palaeoecology*, 576, 110513.
775 <https://doi.org/doi.org/10.1016/j.palaeo.2021.110513>

776 Gilabert, V., Batenburg, S. J., Arenillas, I., & Arz, J. A. (2021b). Contribution of orbital
777 forcing and Deccan volcanism to global climatic and biotic changes across the
778 Cretaceous-Paleogene boundary at Zumaia, Spain. *Geology*, 50, 21–25.
779 <https://doi.org/https://doi.org/10.1130/G49214.1>

780 Gu, X., Zhang, L. M., Yin, R. S., Grasby, S. E., Yao, H. W., Tan, J., & Wang, C. S. (2022).
781 Deccan volcanic activity and its links to the end-Cretaceous extinction in northern
782 China *Global and Planetary Change*, 210, 103772.

783 Harper, D. T., Suarez, M. B., Uglesich, J., You, H. L., Li, D. Q., & Dodson, P. (2021).
784 Aptian-Albian clumped isotopes from northwest China: cool temperatures, variable
785 atmospheric $p\text{CO}_2$ and regional shifts in the hydrologic cycle. *Climate of the Past*,
786 17(4), 1607–1625. <https://doi.org/10.5194/cp-17-1607-2021>

787 Hart, M. B., Leighton, A. D., Hampton, M. C., & Smart, W. (2019). Global bioevents and the
788 Cretaceous/Paleogene boundary in Texas and Alabama: Stratigraphy, correlation and
789 ocean acidification. *Global and Planetary Change*, 175, 129–143.

790 Henehan, M. J., Hull, P. M., Penman, D. E., Rae, J. W., & Schmidt, D. N. (2016).
791 Biogeochemical significance of pelagic ecosystem function: an end-Cretaceous case
792 study. *Philos Trans R Soc Lond B Biol Sci*, 371(1694).
793 <https://doi.org/10.1098/rstb.2015.0510>

794 Henehan, M. J., Ridgwell, A., Thomas, E., Zhang, S., Alegret, L., Schmidt, D. N., Rae, J. W.
795 B., Wits, J. D., et al. (2019). Rapid ocean acidification and protracted Earth system
796 recovery followed the end-Cretaceous Chicxulub impact. *Proceedings of the National*
797 *Academy of Sciences*, 116(45), 22500–22504.
798 <https://doi.org/10.1073/pnas.1905989116>

799 Hildebrand, A. R., Penfield, G. T., Kring, D. A., Pilkington, M., Camargo, A., Jacobsen, S. B.,
800 & Boynton, W. V. (1991). Chicxulub Crater - a Possible Cretaceous Tertiary
801 Boundary Impact Crater on the Yucatan Peninsula, Mexico. *Geology*, 19(9), 867–871.
802 [https://doi.org/10.1130/0091-7613\(1991\)019<0867:Ccapct>2.3.Co;2](https://doi.org/10.1130/0091-7613(1991)019<0867:Ccapct>2.3.Co;2)

803 Hollis, C. J., Taylor, K. W. R., Handley, L., Pancost, R. D., Huber, M., Creech, J. B., Hines, B.
804 R., Crouch, E. M., et al. (2012). Early Paleogene temperature history of the southwest
805 Pacific Ocean: Reconciling proxies and models. *Earth and Planetary Science Letters*,
806 349–350, 53–66. <https://doi.org/doi:10.1016/j.epsl.2012.06.024>

807 Huang, C. M., Retallack, G. J., & Wang, C. S. (2012). Early Cretaceous atmospheric $p\text{CO}_2$
808 levels recorded from pedogenic carbonates in China. *Cretaceous Research*, 33, 42–49.

809 Huang, C. M., Retallack, G. J., Wang, C. S., & Huang, Q. H. (2013). Paleoatmospheric $p\text{CO}_2$
810 fluctuations across the Cretaceous-Tertiary boundary recorded from paleosol
811 carbonates in NE China. *Palaeogeography, Palaeoclimatology, Palaeoecology*, 385,
812 95–105. <https://doi.org/10.1016/j.palaeo.2013.01.005>

813 Hull, P. M., Bornemann, A., Penman, D. E., Henehan, M. J., Norris, R. D., Wilson, P. A.,

- 814 Blum, P., Alegret, L., et al. (2020). On impact and volcanism across the
815 Cretaceous-Paleogene boundary. *Science*, 367(6475), 266–272.
816 <https://doi.org/10.1126/science.aay5055>
- 817 Hull, P. M., & Norris, R. D. (2011). Diverse patterns of ocean export productivity change
818 across the Cretaceous-Paleogene boundary: New insights from biogenic barium.
819 *Paleoceanography*, 26, PA3205.
- 820 Hsü, K. J., & Mackenzie, F. (1985). “A “Strangelove” ocean in the earliest Tertiary” in The
821 Carbon Cycle and Atmospheric CO₂: Natural Variations Archean to Present. In E. T.
822 Sundquist & W. S. Broecker (Eds.), *Geophysical Monograph Series* (pp. 487–492).
823 Washington, D.C: American Geophysical Union. Imbellone, P. A. (2011).
824 Classification of Paleosols. São Paulo, UNESP. *Geociências*, 30(1), 5–13.
- 825 Jung, C., Voigt, S., Friedrich, O., Koch, M. C., & Frank, M. (2013).
826 Campanian-Maastrichtian ocean circulation in the tropical Pacific. *Paleoceanography*,
827 28(3), 562–573. <https://doi.org/10.1002/palo.20051>
- 828 Keller, G. (1988). Extinction, Survivorship and Evolution of Planktic Foraminifera across the
829 Cretaceous Tertiary Boundary at El-Kef, Tunisia. *Marine Micropaleontology*, 13(3),
830 239–263. [https://doi.org/10.1016/0377-8398\(88\)90005-9](https://doi.org/10.1016/0377-8398(88)90005-9)
- 831 Keller, G. (2014). Deccan volcanism, the Chicxulub impact, and the end-Cretaceous mass
832 extinction: Coincidence? Cause and effect? In *Volcanism, Impacts, and Mass*
833 *Extinctions: Causes and Effects* (pp. 57–89): Geological Society of America, Special
834 Paper.
- 835 Keller, G., Adatte, T., Bhowmick, P. K., Upadhyay, H., Dave, A., Reddy, A. N., & Jaiprakash,
836 B. C. (2012). Nature and timing of extinctions in Cretaceous-Tertiary planktic
837 foraminifera preserved in Deccan intertrappean sediments of the Krishnae Godavari
838 Basin, India. *Earth and Planetary Science Letters*, 341–344, 211–221.
- 839 Keller, G., & Lindinger, M. (1989). Stable Isotope, Toc and CaCO₃ Record across the
840 Cretaceous Tertiary Boundary at El-Kef, Tunisia. *Palaeogeography*,
841 *Palaeoclimatology*, *Palaeoecology*, 73(3–4), 243–265.
842 [https://doi.org/10.1016/0031-0182\(89\)90007-2](https://doi.org/10.1016/0031-0182(89)90007-2)
- 843 Keller, G., Mateo, P., Monkenbusch, J., Thibault, N., Punekar, J., Spangenberg, J. E.,
844 Abramovich, S., Ashckenazi-Polivoda, S., et al. (2020). Mercury linked to Deccan
845 Traps volcanism, climate change and the end-Cretaceous mass extinction. *Global and*
846 *Planetary Change*, 194, 103312. <https://doi.org/10.1016/j.gloplacha.2020.103312>
- 847 Keller, G., Punekar, J., & Mateo, P. (2016). Upheavals during the Late Maastrichtian:
848 Volcanism, climate and faunal events preceding the end-Cretaceous mass extinction.
849 *Palaeogeography*, *Palaeoclimatology*, *Palaeoecology*, 441, 137–151.
850 <https://doi.org/10.1016/j.palaeo.2015.06.034>
- 851 Khadkikar, A. S., Chamyal, L. S., & Ramesh, R. (2000). The character and genesis of calcrete
852 in Late Quaternary alluvial deposits, Gujarat, western India, and its bearing on the
853 interpretation of ancient climates. *Palaeogeography*, *Palaeoclimatology*,
854 *Palaeoecology*, 162(3–4), 239–261. [https://doi.org/10.1016/S0031-0182\(00\)00130-9](https://doi.org/10.1016/S0031-0182(00)00130-9)
- 855 Kring, D. A. (2003). Environmental consequences of impact cratering events as a function of
856 ambient conditions on Earth. *Astrobiology*, 3(1), 133–152.
- 857 Kring, D. A. (2007). The Chicxulub impact event and its environmental consequences at the

858 Cretaceous-Tertiary boundary. *Palaeogeography, Palaeoclimatology, Palaeoecology*,
859 255, 4–21.

860 Lee, Y. I. (1999). Stable isotopic composition of calcic paleosols of the Early Cretaceous
861 Hasandong Formation, southeastern Korea. *Palaeogeography, Palaeoclimatology,*
862 *Palaeoecology*, 150(1–2), 123–133. [https://doi.org/10.1016/S0031-0182\(99\)00010-3](https://doi.org/10.1016/S0031-0182(99)00010-3)

863 Li, G., Hirano, H., Batten, D. J., Wan, X. Q., Willems, H., & Zhang, X. Q. (2010).
864 Biostratigraphic significance of spinicaudatans from the Upper Cretaceous Nanxiong
865 Group in Guangdong, South China. *Cretaceous Research*, 31(4), 387–395.
866 <https://doi.org/10.1016/j.cretres.2010.05.003>

867 Li, G. J., & Elderfield, H. (2013). Evolution of carbon cycle over the past 100 million years.
868 *Geochimica et Cosmochimica Acta*, 103, 11–25.
869 <https://doi.org/10.1016/j.gca.2012.10.014>

870 Li, J., Wen, X. Y., & Huang, C. M. (2016). Lower Cretaceous paleosols and paleoclimate in
871 Sichuan Basin, China. *Cretaceous Research*, 62, 154–171.
872 <https://doi.org/10.1016/j.cretres.2015.10.002>

873 Li, X. H., Chen, S. D., Cao, K., Chen, Y. H., Xu, B. L., & Ji, Y. N. (2009). Paleosols of the
874 mid-Cretaceous: A report from Zhejiang and Fujian, SE China. *Earth Science*
875 *Frontiers*, 16(5).

876 Li, X. H., Jenkyns, H. C., Zhang, C. K., Wang, Y., Liu, L., & Cao, K. (2014). Carbon isotope
877 signatures of pedogenic carbonates from SE China: rapid atmospheric $p\text{CO}_2$ changes
878 during middle-late Early Cretaceous time. *Geological Magazine*, 151(5), 830–849.
879 <https://doi.org/10.1017/S0016756813000897>

880 Littler, K., Rohl, U., Westerhold, T., & Zachos, J. C. (2014). A high-resolution benthic
881 stable-isotope record for the South Atlantic: Implications for orbital-scale changes in
882 Late Paleocene-Early Eocene climate and carbon cycling. *Earth and Planetary*
883 *Science Letters*, 401, 18–30. <https://doi.org/10.1016/j.epsl.2014.05.054>

884 Lomax, B., Beerling, D. G., U. J., & Otto-Bliesner, B. L. (2001). Rapid (10-yr) recovery of
885 terrestrial productivity in a simulation study of the terminal Cretaceous impact event.
886 *Earth and Planetary Science Letters*, 192, 137–144.

887 Ma, M. M., Liu, X. M., & Wang, W. Y. (2018). Palaeoclimate evolution across the
888 Cretaceous-Palaeogene boundary in the Nanxiong Basin (SE China) recorded by red
889 strata and its correlation with marine records. *Climate of the Past*, 14(3), 287–302.
890 <https://doi.org/10.5194/cp-14-287-2018>

891 Ma, M. M., Zhang, W. Y., Zhao, M., Qiu, Y., Cai, H., Chen, J., & Liu, X. M. (2022). Deccan
892 traps volcanism implicated in the extinction of non-avian dinosaurs in southeastern
893 China. *Geophysical Research Letters*, 49, e2022GL100342.
894 <https://doi.org/https://doi.org/10.1029/2022GL100342>

895 Machette, M. N. (1985). Calcic soils of the southwestern United States. *Soils and Quaternary*
896 *Geology of the Southwestern United States*, 1–22. <https://doi.org/10.1130/spe203-p1>

897 Mack, G. H., James, W. C., & Monger, H. C. (1993). Classification of paleosols. *Geological*
898 *Society of America Bulletin*, 105, 129–136.

899 MacLeod, N. (1998). Impacts and marine invertebrae extinctions. In M. M. Grady, R.
900 Hutchison, G. J. H. McCall, & D. A. Rothery (Eds.), *Meteorites: Flux with Time and*
901 *Impact Effects* (Vol. 140, pp. 217–246). London, United Kingdom: Geological

902 Society of London.

903 Milligan, J. N., Royer, D. L., Franks, P. J., Upchurch, G. R., & McKee, M. L. (2019). No
904 evidence for a large atmospheric CO₂ spike across the Cretaceous-Paleogene boundary.
905 *Geophysical Research Letters*, *46*, 3462–3472.
906 [https://doi.org/https://doi.org/10.1029/2018GL081215](https://doi.org/10.1029/2018GL081215)

907 Muller, R. D., Sdrolias, M., Gaina, C., Steinberger, B., & Heine, C. (2008). Long-term
908 sea-level fluctuations driven by ocean basin dynamics. *Science*, *319*, 1357–1362.

909 Nordt, L., Atchley, S., & Dworkin, S. (2003). Terrestrial Evidence for Two Greenhouse
910 Events in the Latest Cretaceous. *GSA Today*, *13*(12), 4.
911 [https://doi.org/10.1130/1052-5173\(2003\)013<4:Teftge>2.0.Co;2](https://doi.org/10.1130/1052-5173(2003)013<4:Teftge>2.0.Co;2)

912 Nordt, L., Atchley, S., & Dworkin, S. I. (2002). Paleosol barometer indicates extreme
913 fluctuations in atmospheric CO₂ across the Cretaceous-Tertiary boundary. *Geology*,
914 *30*(8), 703–706. [https://doi.org/10.1130/0091-7613\(2002\)030<0703:Pbiefi>2.0.Co;2](https://doi.org/10.1130/0091-7613(2002)030<0703:Pbiefi>2.0.Co;2)

915 Nordt, L., Dworkin, S., & Atchley, S. (2011). Biogeochemical and ecosystem behavior
916 interpreted from Late Cretaceous and Early Paleocene paleosols and climates in the
917 western interior of North America. *Geological Society of America Bulletin*, *123*,
918 1745–1762.

919 Norouzi, M., Vaziri-Moghaddam, H., & Kalanat, B. (2021). Cretaceous–Paleogene transition
920 interval in the north flank of the Alborz Mountains (N Iran); Planktic foraminiferal
921 biostratigraphy and stable isotopes evidence. *Journal of African Earth Sciences*, *183*,
922 104329. <https://doi.org/10.1016/j.jafrearsci.2021.104329>

923 Odin, G. S., Hurford, A. J., & Montanari, A. (1992). Study of a presumably
924 volcano-sedimentary layer near the Cretaceous-Paleogene boundary in the Central
925 Apennines (Italy). In G. S. Odin (Ed.), *Phanerozoic Time Scale: International Union*
926 *of Geological Sciences Subcommission on Geochronology Bulletin de Liaison* (pp.
927 26–28).

928 Ogg, J. G., Hinnov, L. A., & Huang, C. (2012). Cretaceous. In F. M. Gradstein, J. G. Ogg, M.
929 Schmitz, & G. Ogg (Eds.), *The Geologic Time Scale* (pp. 793–853). Oxford: Elsevier.

930 Ohno, S. (2014). Production of sulphate-rich vapour during the Chicxulub impact and
931 implications for ocean acidification. *Nature Geoscience*, *7*, 279–282.

932 Opdyke, B. N., & Wilkinson, B. H. (1988). Surface Area Control of Shallow Cratonic to
933 Deep Marine Carbonate Accumulation. *Paleoceanography*, *3*(6), 685–703.
934 <https://doi.org/10.1029/PA003i006p00685>

935 Passey, B. H., & Cerling, T. E. (2002). Tooth enamel mineralization in ungulates:
936 Implications for recovering a primary isotopic time-serie. *Geochimica et*
937 *Cosmochimica Acta*, *66*(18), 3225–3234.
938 [https://doi.org/10.1016/S0016-7037\(02\)00933-X](https://doi.org/10.1016/S0016-7037(02)00933-X)

939 Percival, L. M. E., Jenkyns, H. C., Mather, T. A., Dickson, A. J., Batenburg, S. J., Ruhl, M.,
940 Hesselbo, S. P., Barclay, R., et al. (2018). Does large igneous province volcanism
941 always perturb the mercury cycle? Comparing the records of Oceanic Anoxic Event 2
942 and the end-Cretaceous to other Mesozoic events. *American Journal of Science*,
943 *318*(8), 799–860. <https://doi.org/10.2475/08.2018.01>

944 Quillévéré, F., Norris, R. D., Kroon, D., & Wilson, P. A. (2008). Transient ocean warming
945 and shifts in carbon reservoirs during the early Danian. *Earth and Planetary Science*

946 *Letters*, 265(3–4), 600–615. <https://doi.org/https://doi.org/10.1016/j.epsl.2007.10.040>

947 Renne, P. R., Deino, A. L., Hilgen, F. J., Kuiper, K. F., Mark, D. F., Mitchell, W. S., Morgan,
948 L. E., Mundil, R., et al. (2013). Time scales of critical events around the
949 Cretaceous-Paleogene boundary. *Science*, 339(6120), 684–687.

950 Retallack, G. J. (2001). *Soils of the Past--An Introduction to Paleopedolog.* Blackwell
951 Science Ltd, Oxford: Unwin Hyman.

952 Retallack, G. J. (2005). Pedogenic carbonate proxies for amount and seasonality of
953 precipitation in paleosols. *Geology*, 33(4), 333–336. <https://doi.org/10.1130/G21263.1>

954 Retallack, G. J. (2009). Refining a pedogenic-carbonate CO₂ paleobarometer to quantify a
955 middle Miocene greenhouse spike. *Palaeogeography, Palaeoclimatology,*
956 *Palaeoecology*, 281(1–2), 57–65. <https://doi.org/10.1016/j.palaeo.2009.07.011>

957 Robinson, S. A., Andrews, J. E., Hesselbo, S. P., Radley, J. D., Denni, P. F., Harding, I. C., &
958 Allen, P. (2002). Atmospheric pCO₂ and depositional environment from stable-isotope
959 geochemistry of calcrite nodules (Barremian, Lower Cretaceous, Wealden Beds,
960 England). *Journal of the Geological Society*, 159, 215–224.
961 <https://doi.org/10.1144/0016-764901-015>

962 Romanek, C. S., Grossman, E. L., & Morse, J. W. (1992). Carbon Isotopic Fractionation in
963 Synthetic Aragonite and Calcite - Effects of Temperature and Precipitation Rate.
964 *Geochimica et Cosmochimica Acta*, 56(1), 419–430.
965 [https://doi.org/10.1016/0016-7037\(92\)90142-6](https://doi.org/10.1016/0016-7037(92)90142-6)

966 Sandler, A. (2006). Estimates of atmospheric CO₂ levels during the mid-Turonian derived
967 from stable isotope composition of paleosol calcite from Israel. In A. M. Alonso-Zarza
968 & L. H. Tanner (Eds.), *Paleoenvironmental Record and Applications of Calcretes and*
969 *Palustrine Carbonates* (pp. 75–88): Geological Society of America, Special Paper.

970 Schmidt, A., Skeffington, R. A., Thordarson, T., Self, S., Forster, P. M., Rap, A., Ridgwell,
971 A., Fowler, D., et al. (2016). Selective environmental stress from sulphur emitted by
972 continental flood basalt eruptions. *Nature Geoscience*, 9, 77–82.

973 Schoene, B., Eddy, M. P., Keller, C. B., & Samperton, K. M. (2021). An evaluation of
974 Deccan Traps eruption rates using geochronologic data. *Geochronology*, 3, 181–198.
975 <https://doi.org/https://doi.org/10.5194/gchron-3-181-2021>

976 Schoene, B., Eddy, M. P., Samperton, K. M., Keller, C. B., Keller, G., Adatte, T., & Khadri, S.
977 F. R. (2019). U-Pb constraints on pulsed eruption of the Deccan Traps across the
978 end-Cretaceous mass extinction. *Science*, 363(6429), 862–866.
979 <https://doi.org/10.1126/science.aau2422>

980 Schoene, B., Samperton, K. M., Eddy, M. P., Keller, G., Adatte, T., Bowring, S. A., Khadri, S.
981 F. R., & Gertsch, B. (2015). U-Pb geochronology of the Deccan Traps and relation to
982 the end-Cretaceous mass extinction. *Science*, 347(6218), 182–184.
983 <https://doi.org/10.1126/science.aaa0118>

984 Schulte, P., Alegret, L., Arenillas, I., Arz, J. A., Barton, P. J., Bown, P. R., Bralower, T. J.,
985 Christeson, G. L., et al. (2010). The Chicxulub Asteroid Impact and Mass Extinction
986 at the Cretaceous-Paleogene Boundary. *Science*, 327(5970), 1214–1218.
987 <https://doi.org/10.1126/science.1177265>

988 Scotese, C. R. (Cartographer). (2014). Atlas of Late Cretaceous Maps

989 Sepúlveda, J., Wendler, J. E., Summons, R. E., & Hinrichs, K.-U. (2009). Rapid resurgence of

- 990 marine productivity after the Cretaceous-Paleogene mass extinction. *Science*, 326,
991 129–132.
- 992 Shu, L. S., Zhou, X. M., Deng, P., Yu, X. Q., Wang, B., & Zu, F. P. (2014). Geological
993 features and tectonic evolution of Meso-Cenozoic basins in southeastern China.
994 *Geological Bulletin of China*, 23(9–10), 876–884 (in Chinese with English abstract).
- 995 Sinnesael, M., De Vleeschouwer, D., Coccioni, R., Claeys, P., Frontalini, F., Jovane, L.,
996 Savian, J. F., & Montanari, A. (2016). High-resolution multiproxy cyclostratigraphic
997 analysis of environmental and climatic events across the Cretaceous-Paleogene
998 boundary in the classic pelagic succession of Gubbio (Italy). In M. Menichetti, R.
999 Coccioni, & A. Montanari (Eds.), *The Stratigraphic Record of Gubbio: Integrated*
1000 *Stratigraphy of the Late Cretaceous–Paleogene Umbria-Marche Pelagic Basin* (pp.
1001 115–137): Geological Society of America Special Paper.
- 1002 Spicer, R. A., & Collinson, M. E. (2014). Plants and floral change at the
1003 Cretaceous-Paleogene boundary: three decades on. In G. Keller & A. C. Kerr (Eds.),
1004 *Volcanism, Impacts, and Mass Extinctions: Causes and Effects*. 505 (pp. 117–131):
1005 Geological Society of America Special Paper.
- 1006 Sprain, C. J., Renne, P. R., Vanderkluyzen, L., Pande, K., Self, S., & Mittal, T. (2019). The
1007 eruptive tempo of Deccan volcanism in relation to the Cretaceous-Paleogene boundary.
1008 *Science*, 363(6429), 866–870. <https://doi.org/10.1126/science.aav1446>
- 1009 Soil Survey Staff. (1998). *Keys to Soil Taxonomy*. Blacksburg: Pocahontas Press.
- 1010 Thibault, N., Husson, D., Harlou, R., Gardin, S., Galbrun, B., Huret, E., & Minoletti, F.
1011 (2012). Astronomical calibration of upper Campanian-Maastrichtian carbon isotope
1012 events and calcareous plankton biostratigraphy in the Indian Ocean (ODP Hole 762C):
1013 Implication for the age of the Campanian-Maastrichtian boundary. *Palaeogeography,*
1014 *Palaeoclimatology, Palaeoecology*, 337, 52–71.
1015 <https://doi.org/10.1016/j.palaeo.2012.03.027>
- 1016 Tong, Y., Li, Q., & Wang, Y. Q. (2013). An Introduction to recent advance in the study of the
1017 continental Early Paleogene stages in China. *Journal of Stratigraphy*, 37, 428–440 (in
1018 Chinese with English abstract)
- 1019 Tyrrell, T., Merico, A., & Armstrong McKay, D. I. (2015). Severity of ocean acidification
1020 following the end-Cretaceous asteroid impact. *Proceedings of the National Academy*
1021 *of Sciences*, 112, 6556–6561.
- 1022 Vajda, V., McLoughlin, S. (2007). Extinction and recovery patterns of vegetation across the
1023 Cretaceous-Paleogene boundary – a tool for unraveling the causes of the end-Permian
1024 mass extinction. *Review of Palaeobotany and Palynology*, 144, 99–112.
- 1025 Vajda, V., Raine, J. I., & Hollis, C. J. (2001). Indication of global deforestation at the
1026 Cretaceous-Tertiary boundary by New Zealand fern spike. *Science*, 294(5547), 1700–
1027 1702. <https://doi.org/10.1126/science.1064706>
- 1028 Vajda, V., Raine, J. I., Hollis, C. J., & Strong, C. P. (2003). Global effects of the Chicxulub
1029 asteroid impact on terrestrial vegetation—the palynological record from New Zealand
1030 K–T boundary. In P. Claeys (Ed.), *Impact Studies* (pp. 57–74). Berlin:
1031 Springer-Verlag.
- 1032 Vandenberghe, N., Hilgen, F. J., Speijer, R. P., Ogg, J. G., Gradstein, F. M., Hammer, O.,
1033 Hollis, C. J., & Hooker, J. J. (2012). The Paleogene Period. In F. M. Gradstein, O. J.G.,

1034 S. M., & O. G. (Eds.), *The Geologic Time Scale* (pp. 855–921). Oxford: Elsevier B.V.
1035 Vellekoop, J., Esmeray-Senlet, S., Miller, K. G., Browning, J. V., Sluijs, A., van de
1036 Schootbrugge, B., Damste, J. S. S., & Brinkhuis, H. (2016). Evidence for
1037 Cretaceous-Paleogene boundary bolide "impact winter" conditions from New Jersey,
1038 USA. *Geology*, *44*(8), 619–622. <https://doi.org/10.1130/G37961.1>
1039 Whittle, R. J., Witts, J. D., Bowman, V. C., Crame, J. A., Francis, A. E., & Ineson, J. (2019).
1040 Nature and timing of biotic recovery in Antarctic benthic marine ecosystems
1041 following the Cretaceous–Palaeogene mass extinction. *Palaeontology*, *62*(6), 919–
1042 934.
1043 Wilf, P., Johnson, K. R., & Huber, B. T. (2003). Correlated terrestrial and marine evidence for
1044 global climate changes before mass extinction at the Cretaceous-Paleogene boundary.
1045 *Proceedings of the National Academy of Sciences of the United States of America*,
1046 *100*(2), 599–604. <https://doi.org/10.1073/pnas.0234701100>
1047 Woelders, L., Vellekoop, J., Kroon, D., Smit, J., Casadio, S., Pramparo, M. B., Dinares-Turell,
1048 J., Peterse, F., et al. (2017). Latest Cretaceous climatic and environmental change in
1049 the South Atlantic region. *Paleoceanography*, *32*(5), 466–483.
1050 <https://doi.org/10.1002/2016pa003007>
1051 Wright, V. P. (1992). Paleosol Recognition: A guide to early diagenesis in terrestrial settings.
1052 *Development of Sedimentology*, *47*, 591–619.
1053 Zeebe, R. E., Westerhold, T., Littler, K., & Zachos, J. C. (2017). Orbital forcing of the
1054 Paleocene and Eocene carbon cycle. *Paleoceanography*, *32*, 440–465.
1055 <https://doi.org/10.1002/2016PA003054>
1056 Zhang, L. M., Wang, C. S., Wignall, P. B., Kluge, T., Wan, X. Q., Wang, Q., & Gao, Y.
1057 (2018). Deccan volcanism caused coupled $p\text{CO}_2$ and terrestrial temperature rises, and
1058 pre-impact extinctions in northern China. *Geology*, *46*(3), 271–274.
1059 <https://doi.org/10.1130/G39992.1>
1060 Zhang, X. Q., & Li, G. (2010). Discussion on geological age of the Pingling Member of
1061 Shanghu Formation in the Nanxiong Basin, Guangdong province. *Journal of*
1062 *Stratigraphy*, *39*(1), 74–80 (in Chinese with English abstract).
1063 Zhang, X. Q., Lin, J. N., Li, G., & Lin, Q. X. (2006). Non-marine Cretaceous-Paleogene
1064 boundary section at Datang, Nanxiong, northern Guangdong. *Journal of Stratigraphy*,
1065 *30*, 327–340 (in Chinese with English abstract).
1066 Zhang, X. Q., Zhang, X. M., Hou, M. C., Li, G., & Li, H. M. (2013). Lithostratigraphic
1067 subdivision of red beds in Nanxiong Basin, Guangdong, China. *Journal of*
1068 *Stratigraphy*, *37*, 441–451 (in Chinese with English abstract).
1069 Zhao, M. T., Ma, M. M., He, M., Qiu, Y. D., & Liu, X. M. (2021). Evaluation of the four
1070 potential Cretaceous-Paleogene (K-Pg) boundaries in the Nanxiong Basin based on
1071 evidences from volcanic activity and paleoclimatic evolution. *Science China-Earth*
1072 *Sciences*, *64*(4), 631–641. <https://doi.org/10.1007/s11430-020-9736-0>
1073 Zhao, Z. K., Mao, X. Y., Chai, Z. F., Yang, G. C., Zhang, F. C., & Yan, Z. (2009).
1074 Geochemical environmental changes and dinosaur extinction during the
1075 Cretaceous-Paleogene (K/T) transition in the Nanxiong Basin, South China: Evidence
1076 from dinosaur eggshells. *Chinese Science Bulletin*, *54*(5), 806–815.
1077 <https://doi.org/10.1007/s11434-008-0565-1>

1078 Zhao, Z. K., Ye, J., & Li, H. M. (1991). Extinction of the dinosaurs across the
1079 Cretaceous-Tertiary boundary in Nanxiong Basin, Guangdong Province. *Certebrata*
1080 *Palasiatica*, 29, 1–20.
1081

1082 **References From the Supporting Information**

1083 Bemis, B. E., Spero, H. J., Bijma, J., & Lea, D. W. (1998). Reevaluation of the oxygen isotopic
1084 composition of planktonic foraminifera: Experimental results and revised paleotemperature
1085 equations. *Paleoceanography*, 13(2), 150–160. doi:10.1029/98pa00070

1086 Berggren, W. A., Aubry, M. P., van Fossen, M., Kent, K. V., Norris, R. D., & Quillevere, F. (2000).
1087 Integrated Paleocene calcareous plankton magnetobiochronology and stable isotope
1088 stratigraphy: DSDP Site 384 (NW Atlantic Ocean). *Palaeogeography Palaeoclimatology*
1089 *Palaeoecology*, 159(1–2), 1–51. doi:10.1016/S0031-0182(00)00031-6

1090 Boersma, A., Shackleton, N. J., Hall, M., & Given, Q. (1979). Carbon and oxygen isotope records at
1091 DSDP Site 384 (North Atlantic) and some Paleocene paleotemperatures and carbon isotope
1092 variations in the Atlantic Ocean. In A. Kaneps (Ed.), (pp. 695–717). TX, United States, Texas
1093 A & M University, Ocean Drilling Program, College Station: Initial Reports of the Deep Sea
1094 Drilling Project.

1095 Cramer, B. S., Miller, K. G., Barrett, P. J., & Wright, J. D. (2011). Late Cretaceous-Neogene trends in
1096 deep ocean temperature and continental ice volume: Reconciling records of benthic
1097 foraminiferal geochemistry (δO^{18} and Mg/Ca) with sea level history. *Journal of*
1098 *Geophysical Research-Oceans*, 116. doi:10.1029/2011jc007255

1099 Dennis, K. J., Cochran, J. K., Landman, N. H., & Schrag, D. P. (2013). The climate of the Late
1100 Cretaceous: New insights from the application of the carbonate clumped isotope thermometer
1101 to Western Interior Seaway macrofossil. *Earth and Planetary Science Letters*, 362, 51–65.
1102 doi:10.1016/j.epsl.2012.11.036

1103 Katz, M. E., Katz, D. R., Wright, J. D., Miller, K. G., Pak, D. K., Shackleton, N. J., & Thomas, E.
1104 (2003). Early Cenozoic benthic foraminiferal isotopes: Species reliability and interspecies
1105 correction factors. *Paleoceanography*, 18(2), 1024. doi:10.1029/2002pa000798

1106 Larson, R. L., Steiner, M. B., Erba, E., & Lancelot, Y. (1990). Paleolatitudes and tectonic
1107 reconstructions of the oldest portion of the Pacific Plate; a comparative study. In L. H.
1108 Dearthmont & N. K. McQuiston (Eds.), (pp. 615–631). TX, United States, Texas A & M
1109 University, Ocean Drilling Program, College Station: Initial Reports of the Deep Sea Drilling
1110 Project.

1111 Lhomme, N., Clarke, G. K. C., & Ritz, C. (2005). Global budget of water isotopes inferred from polar
1112 ice sheets. *Geophysical Research Letters*, 32(20), L20502. doi:10.1029/2005gl023774

1113 Shackleton, N. J., & Kennett, J. P. (1975). Paleotemperature history of the Cenozoic and the initiation
1114 of Antarctic glaciation; oxygen and carbon isotope analyses in DSDP sites 277, 279, and 281.
1115 *Initial Reports of the Deep Sea Drilling Project*, 29, 743–775.

1116 Westerhold, T., Rohl, U., Donner, B., McCarren, H. K., & Zachos, J. C. (2011). A complete
1117 high-resolution Paleocene benthic stable isotope record for the central Pacific (ODP Site
1118 1209). *Paleoceanography*, 26, PA2216. doi:10.1029/2010pa002092

1119 Wilson, P. A., Norris, R. D., & Cooper, M. J. (2002). Testing the Cretaceous greenhouse hypothesis

1120 using glassy foraminiferal calcite from the core of the Turonian tropics on Demerara Rise.
1121 *Geology*, 30(7), 607–610. doi:10.1130/0091-7613(2002)030<0607:Ttcghu>2.0.Co;2
1122 Zachos, J. C., Stott, L. D., & Lohmann, K. C. (1994). Evolution of Early Cenozoic Marine
1123 Temperatures. *Paleoceanography*, 9(2), 353–387. doi:10.1029/93pa03266
1124

1125 **Figure caption**

1126 Figure 1 Global climate zones laid over the K/PgB (~66 Ma) paleogeographic map (Scotese,
1127 2014). Climate zones are modified from Boucot et al. (2013). Climate-sensitive sedimentary
1128 data are selected from those of the late Maastrichtian to project in the map, which is different
1129 from that of the Coniacian-Maastrichtian climatic zones in Boucot et al. (2013). The data
1130 marked as the Late Cretaceous are not chosen for the Maastrichtian zones. Please note, some
1131 climatic boundary lines are adjusted from the map in Boucot (2013). 1, Datang section,
1132 Nanxiong Basin, South China (this work); 2, core of Well Songke #1, Songliao Basin,
1133 Northeast China (Gao et al., 2015, 2021; Zhang et al., 2018); 3, Dawson Creek section of the
1134 Tornillo Basin, Big Bend National Park, Texas, USA (Nordt et al., 2003).
1135

1136 Figure 2 Geological sketches of the Nanxiong Basin with the location of the observed
1137 section. A, Geographical map of China showing the localities of study and citation sections. B,
1138 Geological sketch of the Nanxiong Basin. Geological map simplified from Shu et al. (2004).
1139 C, Geological sketch and transportation nearby the Datang section, Nanxiong, intercepted and
1140 simplified from Zhang et al. (2013).
1141

1142 Figure 3 Log of the Datang section, Nanxiong of Guangdong showing the stratigraphy,
1143 positions of calcrete samples and results of carbon and oxygen isotopes and estimated $p\text{CO}_2$.
1144 Magneto-chronostratigraphy are cited from Clyde et al. (2010) and lithostratigraphy and
1145 thickness from Zhang et al. (2006). Ages marked as red bold numbers aside the log are
1146 obtained by the chronostratigraphy chart (Ogg et al., 2012; Vandenberghe et al., 2012). Please
1147 note, the strongest negative excursion occurs at the K/PgB in the Datang section.
1148 Uncertainties (errors) of $p\text{CO}_2$ are produced from the subtraction from $S_{(z)}=2000$ ppmV at 25°C
1149 using the method developed by Breecker and Retallack (2014) (details see section 4 in text).
1150

1151 Figure 4 Field paleosol photos and microscopic CL images from the upper Upper
1152 Cretaceous-Paleogene at the Datang section, Nanxiong, Guangdong province. A, Close-up
1153 view of calcisol with ginger-like and irregular calcretes at horizon of the sample DT-02, upper
1154 Zhutian Formation. B, Close-up view of calcisol with the calcrete at horizon of the sample
1155 DT-84, middle Shanghu Formation. C, CL image of the calcrete sample DT-55, lower
1156 Shanghu Formation. D, CL image of the calcrete sample DT-72, middle Shanghu Formation.
1157

1158 Figure 5 Crossplot of carbon and oxygen isotopes of the latest Cretaceous-earliest
1159 Paleogene pedogenic carbonates from the Datang section, Nanxiong Basin, South China.
1160

1161 Figure 6 Stable isotopes of terrestrial and marine carbonate, sea-water temperature and
1162 $p\text{CO}_2$ in the late Late Cretaceous-early Paleocene (~70–62 Ma). A, Carbon isotope of marine

1163 fossil carbonates. **B**, Carbon isotope of pedogenic carbonates (details refer to Table S1–S2). **C**,
1164 $p\text{CO}_2$ estimated by carbon isotope of pedogenic carbonates (Table S1–S2). **D**, BWT and SST
1165 from ocean records (Text S1 and Table S3). Kernel smoothed time series (thick dark red dash
1166 lines) were calculated using a fixed 0.25 Myr bandwidth and using an Epanechnikov kernel
1167 centered on each data point. Note, three phases of carbon cycles and $p\text{CO}_2$ from terrestrial
1168 pedogenic carbonates are identified.

1169

1170 Figure 7 Comparison of $\delta^{13}\text{C}$, $p\text{CO}_2$ and SST across the K/PgB. Carbon isotopes of bulk
1171 carbonates marked as blue squares (ODP Site 1267, Walvis Ridge, South Atlantic) and grey
1172 circles (ODP Site U1403, J-Anomaly Ridge, North Atlantic) in the figure 7A are from [Hull et](#)
1173 [al. \(2020\)](#). Thick grey lines are five-point smoothed curves. The Deccan Trap ranges
1174 66.3–65.6 Ma ([Schoene et al., 2015, 2019](#)) with a precise alternative $^{40}\text{Ar}/^{39}\text{Ar}$ age
1175 66.413–65.422 Ma (dash line limitation with red arrow. [Sprain et al., 2019](#)) and corrected
1176 eruption rate (brownish red shadow area. [Schoene et al., 2021](#)). Other symbols and relevant
1177 data refer to Fig. 6.

1178

1179 **Supplementary data caption**

1180 **Text S1.** Cited marine C-O isotopes and recalibrated seawater temperatures

1181

1182 **Table S1.** Details of samples, C-O isotope composition and $p\text{CO}_2$ of the latest
1183 Cretaceous-earliest Paleocene (~70–62 Ma) at Datang section, Nanxiong of Guangdong, SW
1184 China. GCD is the main part between Yangmeikeng and Huashuxia in the Datang section
1185 ([Zhao et al., 1991](#)).

1186

1187 **Table S2.** Details of samples, C-O isotope composition and $p\text{CO}_2$ of the latest
1188 Cretaceous-earliest Paleocene (~70–62 Ma) compiled from GCD section, Nanxiong, S China;
1189 Songke Well #1, Songliao Basin, NE China and Dawson Creek, Texas, America

1190

1191 **Table S3.** C-O isotopes, SST and BWT of the latest Cretaceous-earliest Paleocene (~70–62
1192 Ma)

1193

1194

Figure 1.

66 Ma, K/Pg boundary



Panthalassa
(Paleo-Pacific)

Panthalassa
(Paleo-Pacific)

Sea Level +80m
Mollweide Projection

- Evaporite
- ▲ Calcrete
- ▲ Laterite
- Kaolinite
- Coal

Figure 2.

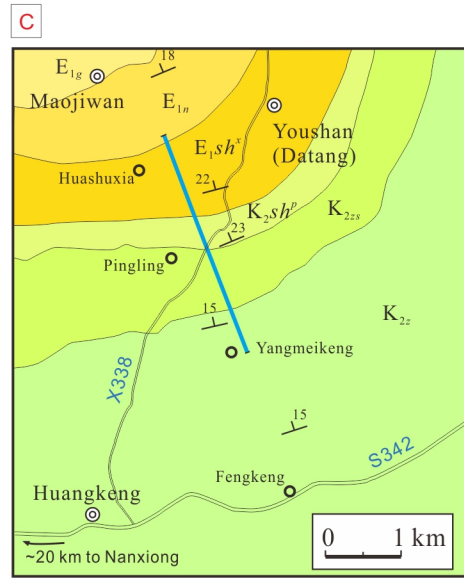
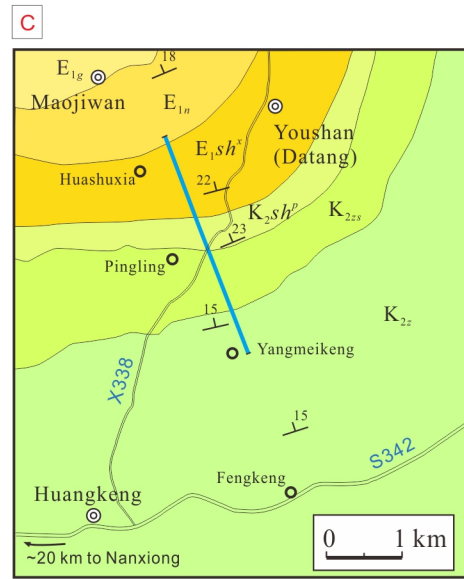
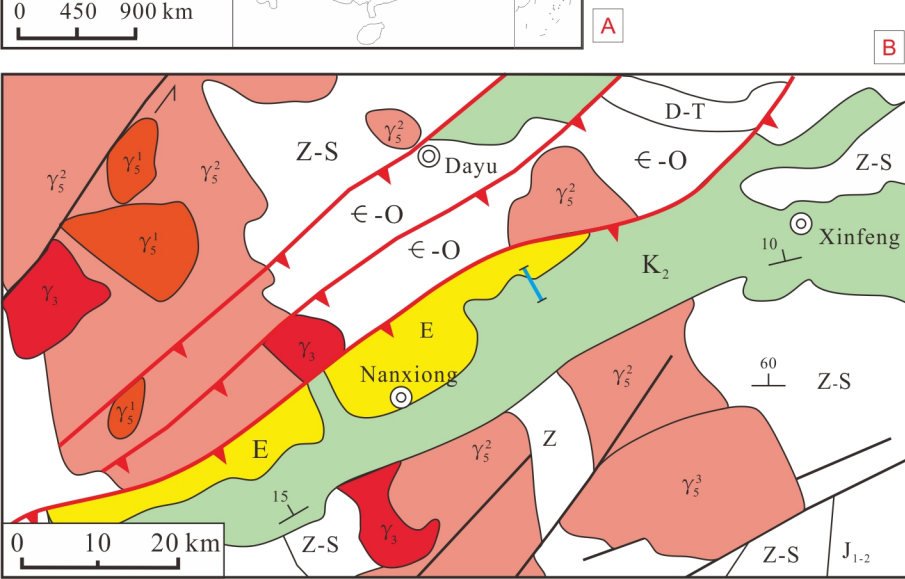
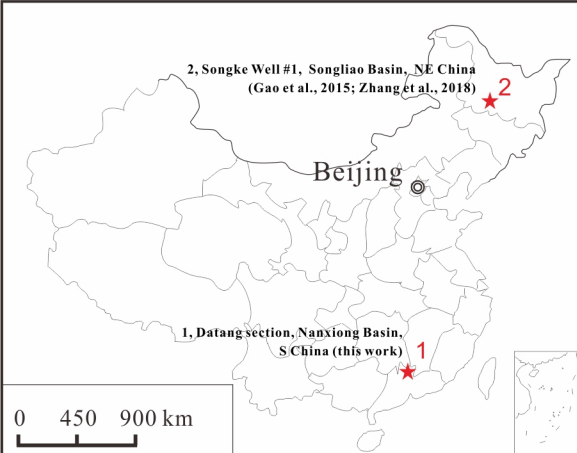


Figure 3.

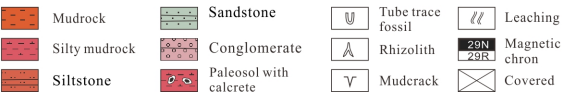
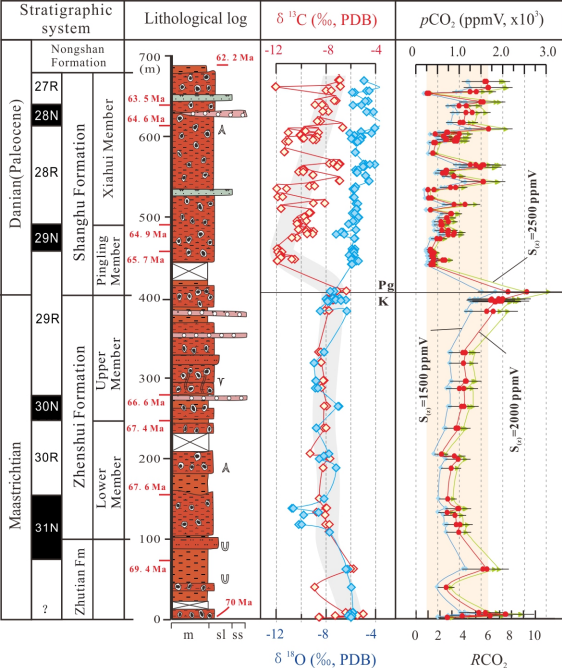


Figure 4.

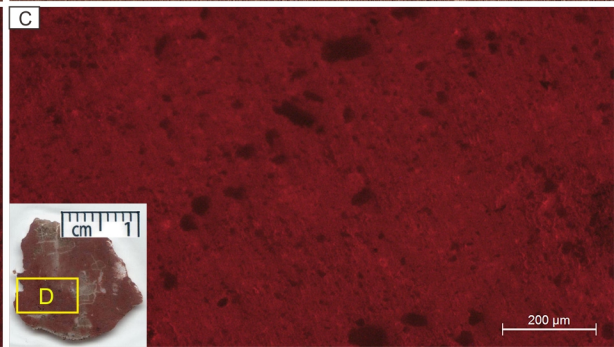
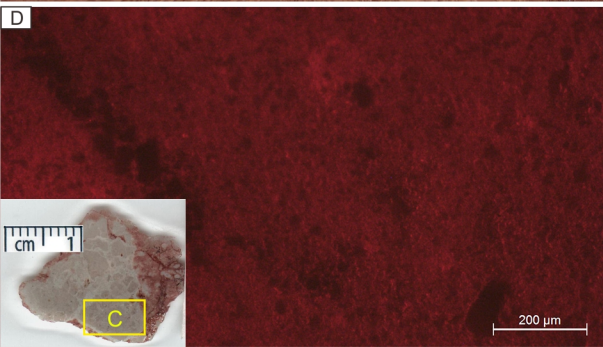


Figure 5.

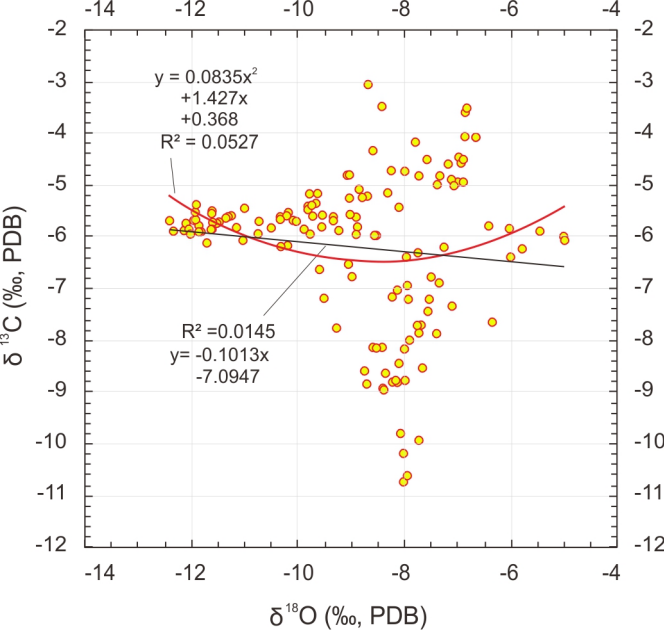


Figure 6.

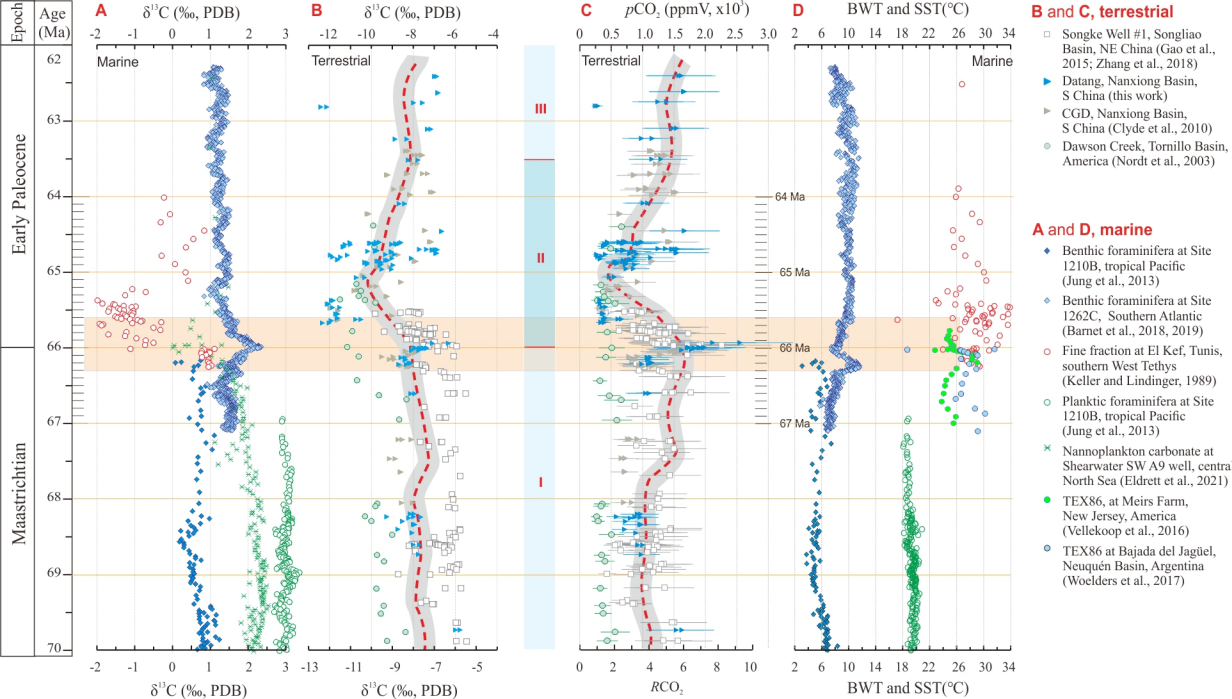


Figure 7.

